

Washington University in St. Louis

Washington University Open Scholarship

McKelvey School of Engineering Theses & Dissertations

McKelvey School of Engineering

Summer 8-15-2017

Minimum Induced Power for a Helicopter in High-Speed Forward Flight

Junsoo (sean) Hong
Washington University in St. Louis

Follow this and additional works at: https://openscholarship.wustl.edu/eng_etds



Part of the [Aerospace Engineering Commons](#), and the [Mechanical Engineering Commons](#)

Recommended Citation

Hong, Junsoo (sean), "Minimum Induced Power for a Helicopter in High-Speed Forward Flight" (2017).
McKelvey School of Engineering Theses & Dissertations. 320.
https://openscholarship.wustl.edu/eng_etds/320

This Dissertation is brought to you for free and open access by the McKelvey School of Engineering at Washington University Open Scholarship. It has been accepted for inclusion in McKelvey School of Engineering Theses & Dissertations by an authorized administrator of Washington University Open Scholarship. For more information, please contact digital@wumail.wustl.edu.

WASHINGTON UNIVERSITY IN ST. LOUIS

Mechanical Engineering & Materials Science

Dissertation Examination Committee:

David Peters, Chair

Philip Bayly

Humberto Gonzalez

Swami Karunamoorthy

Mark Meacham

Minimum Induced Power for a Helicopter in High-Speed Forward Flight

by

JunSoo (Sean) Hong

A dissertation presented to
The Graduate School
of Washington University in
partial fulfillment of the
requirements for the degree
of Doctor of Philosophy

August 2017
St. Louis, Missouri

© 2017, JunSoo (Sean) Hong

Table of Contents

List of Figures	vi
List of Symbols	ix
Acknowledgement	xi
Abstract	xiii
1. Introduction.....	1
1.1 Problem Statement	1
1.2 Previous Work.....	2
- Glauert (1927).....	2
- Harris (1987).....	3
- Hall, Yang, and Hall (1994)	4
- Hall and Hall (2010)	4
- Ormiston (2004 - 2013)	6
1.3 Work with Finite-state Inflow Model.....	7
- Cristina Garcia-Duffy (2008)	8
- Chad File (2013)	10
1.4 Present approach	11
2. Infinite Number of Blades	13
2.1 Finite-State Inflow Theory	13
2.2 Induced Power Formulation	14

2.3 Rotor Loads in Terms of Pressure Expansions	15
2.4 Blade Pitch Angle in Terms of Rotor Control.....	16
2.5 Blade Element Lift in Terms of Rotor Pitch and Inflow	17
2.6 Pressure Expansions in Terms of Rotor Control and Inflow Feedback	18
2.7 Reverse Flow	20
3. Finite Number of Blades	23
3.1 Finite-State Inflow Theory	23
3.2 Induced Power Formulation	24
3.3 Pressure Expansions in Terms of Rotor Control with Inflow Feedback.....	25
3.4 Reverse Flow with a Finite Number of Blades	28
4. Optimization	30
4.1 Infinite Number of Blades.....	30
4.2 Finite Number of Blades without Inflow Coupling	32
4.3 Finite Number of Blades with Inflow Coupling.....	33
4.4 Normalization of the Power Equation	34
4.5 Solution Convergence Methods	35
5. Results with an Infinite Number of Blades.....	36
Induced Power Results with Classical Control	36
Without Reverse Flow	37
Effect of Reverse Flow	38

Effect of Inflow Feedback and Reverse Flow.....	41
Induced Power Results with Higher Harmonic Control.....	42
Without Reverse Flow	42
Effect of Reverse Flow and Inflow Feedback.....	43
Effect of Inflow Feedback and Reverse Flow.....	44
Magnitude of Optimum Blade Pitch with Realistic Thrust.....	45
Non-Dimensional Pressure and Inflow Distributions	46
6. Results with a Finite Number of Blades	49
Comparisons of Results with Hall and Hall ⁴ , Hall and Giovanetti ¹⁶ , and Ormiston ⁹	49
Results with Classical Control	52
Without Reverse Flow	52
Effect of Reverse Flow and Inflow Feedback.....	54
Comparison between Finite and Infinite Numbers of Blades	55
Results with Higher Harmonic Controls	55
Non-Dimensional Pressure and Inflow Distributions	57
6. Summary and Conclusions	61
7. Possible Future Work.....	62
References	64
Appendices.....	67
Appendix A. Table Method and Rectangular Method	67

Appendix B. Real Notation to Complex Notation 70

 Inflow Distributions 70

 Pressure Distributions 71

 Rotor Controls..... 71

 D Matrix..... 72

Appendix C. Simplification of Eq. (2.6.5) to Eq. (2.6.7)..... 72

Appendix D. Determinant of Wheatley Terms 74

List of Figures

Figure 1.1. Power coefficient data from Harris.	3
Figure 1.2. Hall and Hall ⁴ minimum induced power for trimmed rotors at 0- and -5-deg angle of attack.	5
Figure 1.3. Hall and Hall ⁴ net circulation contours of 4-bladed trimmed rotor.....	5
Figure 1.4. Three-bladed trimmed rotor results of Ormiston ⁹ with the reverse-flow and inflow feedback effect	6
Figure 1.5. Garcia-Duffys's comparison between finite-state and Betz's distribution, Ref. [11].....	8
Figure 1.6. Garcia-Duffy's finite-state results validation with Goldsein's and Prandtl's circulation distribution, Ref. [11].....	8
Figure 1.7. Axial, skewed, and perfectly edgewise flow figures.....	9
Figure 1.8. File's induced power results, Ref. [15].	10
Figure 2.1. Unsteady and steady parts of the dynamic wake model.....	13
Figure 3.1. Unsteady form of dynamic wake model.....	23
Figure 4.1. Rectangular and table convergence methods	35
Figure 5.1. Fully converged induced power without reverse flow, M=3.	37
Figure 5.2. Effect of root cut-out without reverse flow, M=3, N=100.	37
Figure 5.3. Non-dimensional pressure distribution across the disk with rco=0.1, $\mu=0.9$, N=100.	38
Figure 5.4. Pressure distribution across the disk with rco=0.4, $\mu=0.9$, N=100.	38
Figure 5.5. Effect of root-cutout with reverse flow, no inflow feedback, M=3, N=100.	39
Figure 5.6. Pitch angle with and without reverse flow.	40
Figure 5.7. Non-dimensional pressure distribution across the rotor with reverse flow.	40

Figure 5.8. Effect of inflow feedback with reverse flow, no root cutout, $M=3$, $N=100$	41
Figure 5.9. Effect of HHC control without reverse flow, no root cutout, $N=100$	42
Figure 5.10. Effect of HHC control with reverse flow, no root cutout, $N=10$	43
Figure 5.11. Non-dimensional pressure distribution across the disk with reverse flow, $H=1$, $N=10$, $\mu=0.8$	43
Figure 5.12. Non-dimensional pressure distribution across the disk with reverse flow, $H=2$, $N=10$, $\mu=0.8$	43
Figure 5.13. Effect of HHC control with reverse flow and inflow feedback, no root cutout, solidity=0.15, $N=10$	44
Figure 5.14. Realistic blade pitch without (left) and with (right) reverse flow using conventional collective cyclic pitch control to trim, and three advance ratios.....	45
Figure 5.15. Non-dimensional pressure distributions with and without reverse flow, for three advance ratios.....	46
Figure 5.16. Non-dimensional inflow distribution with and without reverse flow, for three advance ratios.....	48
Figure 6.1. Rubber blade minimum induced power comparison between present and Hall and Hall ⁴ , $M:60$, $rco: 0.1$	50
Figure 6.2. Comparing induced power results with Hall and Giovanetti ¹⁶ , $Q:4$, $M:12$, $rco:0.1$, $\sigma: 0.1157$	51
Figure 6.3. Comparison of induced power results with Ormiston ⁹ , $Q:3$, $M:12$, $rco:0$, $\sigma: 0.111$..	51
Figure 6.4. Induced power without reverse flow for varied blade numbers and solidity values, $M:12$, $rco:0$	52
Figure 6.5. Pressure distribution with narrower solidity.....	53

Figure 6.6. Pressure distribution with wider solidity.	53
Figure 6.7. Induced power with reverse flow effect for varied blade numbers and solidity, M:12, rco:0	54
Figure 6.8. Induced power with reverse flow and inflow feedback effects for varied blade numbers and solidity, M:12, rco:0.	54
Figure 6.9. Effects of assumptions on induced power, Q:4, M:12, rco:0, σ : 0.1.	55
Figure 6.10. Effects of assumptions on induced power, Q: ∞ , M:12, rco:0, σ : 0.1.....	55
Figure 6.11. The effect of HHC on induced power without reverse flow and inflow feedback, Q:4, M:12, rco:0, σ : 0.1.....	56
Figure 6.12. The effect of HHC on induced power with reverse flow and inflow feedback, Q:4, M:12, rco:0, σ : 0.1.....	56
Figure 6.13. Pressure distributions both without and with reverse flow, μ = 0.4.....	57
Figure 6.14. Pressure distributions both without and with reverse flow, μ = 0.8.....	58
Figure 6.15. Inflow distribution both without and with reverse flow, μ = 0.4.	59
Figure 6.16. Inflow distribution both without and with reverse flow, μ = 0.8.	60
Figure A.1. How to choose states for table method.....	68
Figure A.2. How to choose states for rectangular method.....	68
Figure A.3. Table method convergence without reverse flow for an infinite number of blades ..	69
Figure A.4. Rectangular method convergence without reverse flow for an infinite number of blades	69

List of Symbols

a	slope of lift curve, rad^{-1}
A	rotor disk area
$[A]$	effect of control input
$[\bar{A}]$	effect of control input with inflow coupling
$[B]$	effect of inflow feedback without coupling
$[\bar{B}]$	effect of inflow feedback with coupling
$\{C\}$	rotor loading constraints
$\{\bar{C}\}$	normalized loading constraints, $\{C\}/C_T$
c	blade chord
C_L	roll moment coefficient
C_M	pitch moment coefficient
C_P	induced power coefficient
C_T	thrust coefficient
D	maximum order of blade radial twist control polynomial
$[D]$	matrix relating pressure states to rotor loads
$F()$	functional
H	maximum harmonic of blade pitch control
$[I]$	identity matrix
L	total lift, L_q/Q
L_q	lift per unit length on q-th blade
$[L]$	matrix relating pressure states to inflow states
$[L]_{\text{sym}}$	symmetric part of $[L]$
M	maximum harmonic number of inflow states
N	number of polynomials used in the expansion of radial inflow function
ΔP	non-dimensional pressure difference
$P_n^m(\nu)$	normalized Legendre function
$[P]$	matrix relating pressure states to control variables without inflow coupling
$[\bar{P}]$	matrix relating pressure states to control variables with inflow coupling
Q	number of blades
R	blade radius, m
rco	root cutout, fraction of blade radius
\bar{r}	non-dimensional radial position
t	non-dimensional time
$[U]$	flipping matrix
U_T	blade section tangential velocity component, m/sec
U_P	blade section perpendicular velocity component, m/sec
V	total non-dimensional velocity, $\sqrt{\mu^2 + \lambda^2}$
V_∞	non-dimensional free-stream velocity
$w(\bar{r}, \psi)$	non-dimensional induced flow
α_s	nose up shaft angle, rad
$\{\gamma\}$	inflow states
$\theta(\bar{r}, \psi)$	blade pitch angle, rad

$\{\theta\}$	rotor control
λ	inflow due to shaft tilt = $-\mu\alpha$
$\{\Lambda\}$	Lagrange multiplier
μ	advance ratio = $V\sin(\chi)$
ν	ellipsoidal coordinate
ρ	air density, kg/m ³
σ	solidity, $Qc/\pi R$
$\{\tau\}$	pressure states
$\phi_n^m(\bar{r})$	inflow expansion function
χ	wake skew angle, rad
ψ	azimuth angle, rad
Ω	rotor speed, rad/sec
(\cdot)	derivative with respect to non-dimensional time

Acknowledgement

This work was sponsored by the GeorgiaTech/Washington University Rotorcraft Center of Excellence RCOE through a Grant from the Joint Rotorcraft Program, Dr. Mahendra Bhagwat Technical Monitor.

JunSoo (Sean) Hong

Washington University in St. Louis

August 2017

Dedicated to my parents.

Abstract

Minimum Induced Power for a Helicopter in High-Speed Forward Flight

by

JunSoo (Sean) Hong

Doctor of Philosophy in Mechanical Engineering

Washington University in St. Louis, 2017

Research Advisor: Professor David A. Peters, Chair

A dynamic inflow model is used to calculate minimum induced power for a helicopter in high-speed forward flight with infinite and finite number of blades. Comparisons between analytical and numerical results are shown and they show good agreement. Different flow conditions (such as with and without reverse flow or inflow feedback) are used to show how each condition affects optimum induced power. Several results confirm the findings of earlier investigations such as a singularity in rotor power in reverse flow and induced power reduction with increase in blade number. Some of the new findings are that greater inflow feedback (due to greater solidity) reduces the induced power for an infinite-bladed rotor. For a rotor with a finite number of blades, the addition of inflow feedback can either increase or decrease optimum power depending on the flight conditions. Results obtained using higher harmonic blade pitch control show that induced power can be thereby reduced for all conditions.

1. Introduction

1.1 Problem Statement

The power necessary to fly a helicopter can be divided into three components: parasite power, profile power, and induced power. Both parasite and profile power are related to skin friction drag. Therefore, minimization of parasite and profile power mainly focuses on modification of the fuselage and airfoil respectively. In contrast, induced power is not affected by skin friction drag, rather depends on the manner in which pressure and inflow are distributed across the rotor disk. Listed below are some factors that can influence inflow and pressure distributions.

1. reverse flow
2. inflow feedback
3. amount of control
4. amount of root-cutout
5. number of blades

This dissertation investigates how these factors affect the induced power necessary to fly a helicopter in high-speed forward flight and how this power can be minimized. Minimization of induced power is important because it directly affects fuel consumption, maximum payload, and the maximum forward speed of a helicopter. Reduction in power leads to a more fuel-efficient, faster rotorcraft that can carry increased payload. Therefore, many researchers have searched for ways to minimize the induced power in high-speed forward flight.

Throughout this dissertation, non-dimensional parameters are used to give a general understanding of rotor power. The advance ratio, μ , is the ratio of the inplane component of forward speed to the tip speed of a rotor:

$$\mu = \frac{V_{\infty}}{\Omega R} = \frac{\text{forward speed}}{\text{tip speed}} \quad (1.1.1)$$

1.2 Previous Work

- Glauert (1927)

Glauert used classical momentum theory to obtain the ideal induced power for helicopters at a high advance ratio (i.e., the minimum induced power possible), Ref. [1]. He assumed an infinite number of blades and a uniform inflow distribution to obtain the following result:

$$\left(\frac{C_P}{C_T^2} \right)_{\text{Glauert}} = \frac{1}{2\mu} \quad (1.2.1)$$

The ideal normalized induced power decreases as the advance ratio increases. Equation (1.2.1) sets the lowest possible limit for an induced power. It follows that the actual induced power of a realistic rotor must be greater than this value.

- Harris (1987)

In Ref. [2], Harris emphasized the induced power by stating that the rotor performance at a high advance ratio is more seriously eroded by induced drag than by blade stall and/or compressibility losses. He obtained realistic induced power behavior from runs of CAMRAD, which is NASA's flight simulation code based on a free-wake analysis.

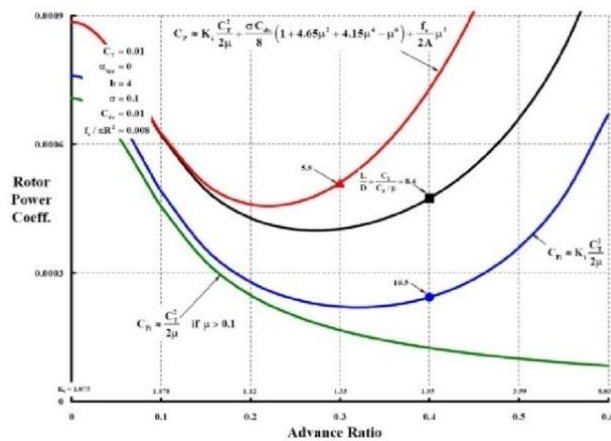


Figure 1.1. Power coefficient data from Harris.

In Fig. 1.1 the red curve is the total power of the helicopter. Subtraction of the parasite power from the total power gives the black curve, and subtraction of both the parasite and profile powers gives the blue curve. A comparison of the blue and green curves gives an idea of how far off the actual power is from the ideal power for a realistic helicopter. Note that the gap between these two lines increases as the advance ratio increases. At an advance ratio of 0.6, the realistic induced power is almost seven times higher than ideal induced power.

Glauert's ideal assumptions of uniform inflow and an infinite number of blades give good results for hover and low speed flight. However, these assumptions seem not to be adequate for high-speed flight. This is in sharp contrast to the fixed-wing arena, in which planes can come within 85% to 95% of ideal efficiency. Harris asked the aerodynamic community to find out why

there is such a gap between the ideal and actual induced power for rotors and to also determine if design changes could recover some of this lost power. This challenge is the motivation for the present research.

- Hall, Yang, and Hall (1994)

In 1994, Hall et al. found the optimum circulation distributions that minimized the rotor induced power in both axial and skewed flow, Ref. [3]. (Lift is easily obtained from the circulation.) Therefore, they provided a first step towards what Harris requested in Ref. [2]. Hall et al. used the vortex lattice and finite element methods as their near and far wake analyzing tools, respectively. First, they compared their axial flow results with Goldstein's propeller theory and successfully matched their optimum bound circulation distribution to Goldstein's. Then, they calculated optimum lift distribution and induced power for a 3-bladed rotor at an advance ratio of 0.25. The optimum rotor had 22-24 % less induced power than the non-optimum rotor, Ref. [3].

- Hall and Hall (2010)

In 2010, Hall and Hall computed both the optimum induced and profile powers with varying blade numbers and advance ratios. The rotor was assumed to be trimmed, meaning that the rotor was set to a given thrust coefficient with zero roll and pitch moment. Hall and Hall used what they called a "rubber rotor", in which any lift (circulation) distribution is assumed to be possible. This optimum circulation distribution was used to produce the results in Figs. 2 and 3.

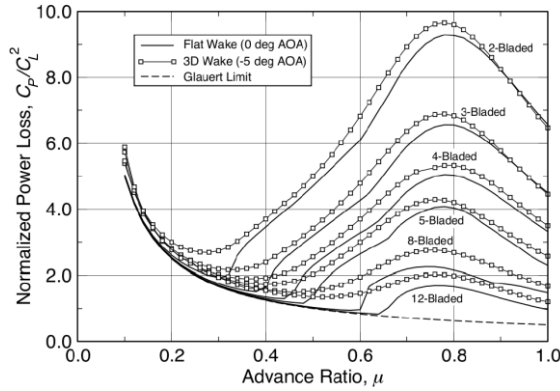


Figure 1.2. Hall and Hall⁴ minimum induced power for trimmed rotors at 0- and -5-deg angle of attack.

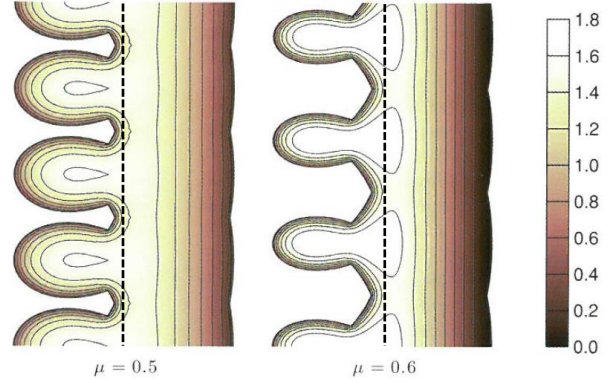


Figure 1.3. Hall and Hall⁴ net circulation contours of 4-bladed trimmed rotor.

As shown in Fig. 1.2, induced power increases as the number of blades decreases. A marked increase in induced power is found between advance ratios of 0.7 and 0.8, regardless of the number of blades. Hall and Hall explained that this increase in induced power is caused by gaps in the wake on the retreating side of the rotor.

Figure 1.3 illustrates the circulation contours of the flat wake sheet behind a rotor with $\chi = 90^\circ$ for the two advance ratio cases. Black vertical dotted lines are added to the original figure from Ref. [4] to clarify that the left side is the retreating and the right side is the advancing. One full complete turn of a four-bladed rotor wake is captured. Since a four-bladed rotor was used to produced Fig. 1.3, the retreating side has four distinctive wake patterns. Figure 1.3 shows that the distance between the gaps increases as the advance ratio increases from 0.5 to 0.6. As the number of blades is decreased and as the advance ratio approaches 0.7-0.8, the distance between the gaps becomes larger, which reduces the efficiency of the rotor.

Figure 1.2 provides a more realistic limit for the induced power than Glauert's formula does, but some non-realistic assumptions are used in the "rubber rotor" model. Obviously, no real rotor

blade assembly could produce arbitrary lift as a function of radius and rotational time along each and every blade.

Optimum circulation distributions that minimize the total power were also obtained in Ref. [4]. The results showed that the viscous effect had little influence on the optimum circulation distribution. This conclusion emphasizes that the inviscid component of total power is larger than the profile component.

- Ormiston (2004 - 2013)

Ormiston calculated and optimized induced power using RCAS (Rotorcraft Comprehensive Analysis System), Refs. [5] - [9]. A three-bladed rotor was used to generate the plot shown in Fig. 1.4, and the rotor control used was more realistic than the “rubber rotor” used by Hall and Hall in Ref. [4].

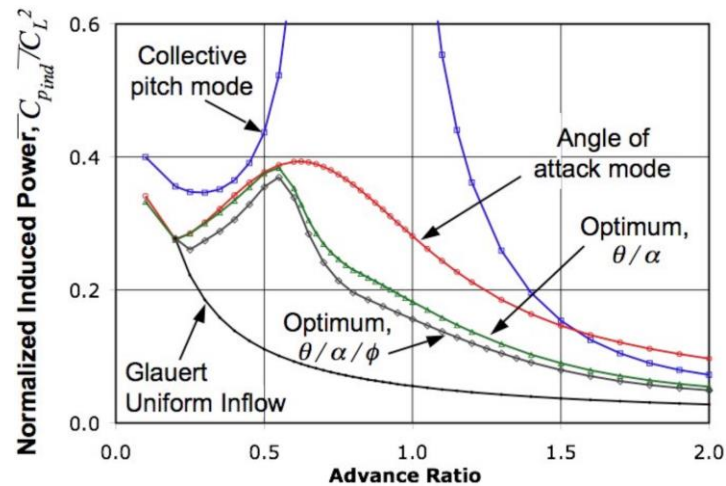


Figure 1.4. Three-bladed trimmed rotor results of Ormiston⁹ with the reverse-flow and inflow feedback effect

In Fig. 1.4 the blue curve was plotted using conventional collective and cyclic pitch control to trim the rotor. Similar to the results obtained by Hall and Hall, the induced power increases near an advance ratio of 0.8. However, in the Ormiston results, the power increases to an infinite value at this critical advance ratio. One can conclude that when reverse flow is included in the power analysis of a trimmed rotor, and when conventional collective and cyclic pitch control are used, the rotor cannot maintain a trimmed condition with finite power in a critical advance ratio range. Therefore, the inability to trim causes the infinite induced power peak shown in Fig. 1.4.

Ormiston found several ways to reduce this infinite induced power peak. One way was to use shaft angle of attack to trim the rotor. That result is shown as the red curve in Fig. 1.4. Ormiston optimized the induced power by combining collective pitch, angle of attack, and twist mode to generate the black line above the Glauert uniform inflow curve line in Fig. 1.4.

1.3 Work with Finite-state Inflow Model

The results of Harris, Hall and Hall, and Ormiston were all obtained from numerical work. Even though Glauert's ideal induced power model was a fully analytical work, a better approximation of induced power was needed in analytical research fields. Therefore, Peters and his students found a way to minimize the induced power analytically by using a finite-state inflow model [10-15]. Using this model was computationally less expensive than most numerical methods. Also, physical insights could be obtained from the results, because the finite-state inflow model was derived from first principles.

- Cristina Garcia-Duffy (2008)

Duffy and Peters developed a quadratic optimization method with a finite-state inflow model, Ref. [10]. To validate the outcome of this method, they compared their results to four well established axial flow results.

- | | | |
|---|---|---|
| 1) actuator disk with infinite number of blades | ↔ | momentum theory |
| 2) actuator disk with finite number of blades | ↔ | Prandtl's results |
| 3) lifting rotor with infinite number of blades | ↔ | Betz's distribution |
| 4) lifting rotor with finite number of blades | ↔ | Prandtl's approximation to Goldstein's solution |

The difference between the actuator disk and lifting rotor model is that the latter includes the energy loss due to swirl velocity. Actuator disk theory neglects this effect, while lifting rotor theory includes it. The Peters-He inflow model was an actuator disk model in its original form, which was developed in 1989, Ref. [12]. In 2005, Makinen and Peters added a swirl correction factor to the Peters-He inflow model to create a lifting rotor model, Ref. [13]. Garcia-Duffy used both the original and modified Peters-He models to validate her optimum induced power result in axial flow. Figures 1.5 and 1.6 give validation examples.

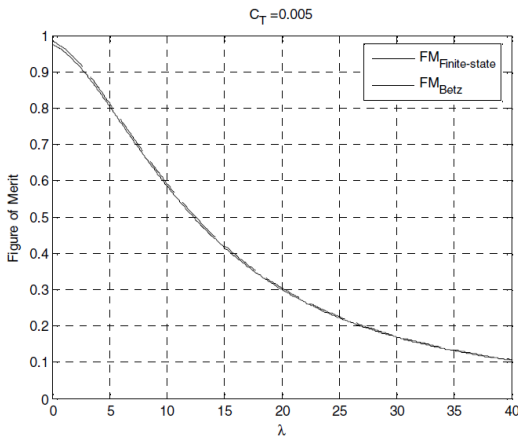


Figure 1.5. Garcia-Duffy's comparison between finite-state and Betz's distribution, Ref. [11].

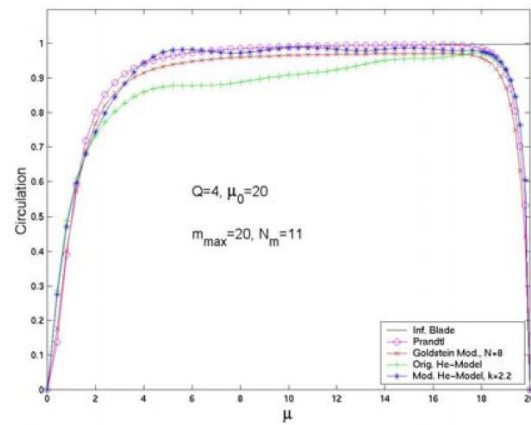


Figure 1.6. Garcia-Duffy's finite-state results validation with Goldstein's and Prandtl's circulation distribution, Ref. [11].

As seen from Figs. 1.5 and 1.6, the optimized results from a finite-state inflow model match well with other results. Knowing that the method worked for the axial flow condition, Duffy moved on to calculate optimum results for skewed flow conditions.

As a first attempt at skewed flow induced power optimization, Duffy used an untrimmed “rubber rotor” with an infinite number of blades. An untrimmed condition means allowing arbitrary rolling and pitching moments during power optimization. Normally, for a rotor to have balanced flight in a skewed flow, the rotor needs to be trimmed, which implies the rolling and pitching moments are equal to zero. Thus, the rotor can only be untrimmed if there are other, external aerodynamic devices, such as wing and auxiliary rotors, that can provide the trimming forces. In the absence of these, then the rotor itself must be trimmed internally.

Garcia-Duffy varied inflow skew angles from 0 to 90 degrees, with 0 degrees indicating an axial flow, and close to 90 degrees indicating a perfectly edgewise flow condition.

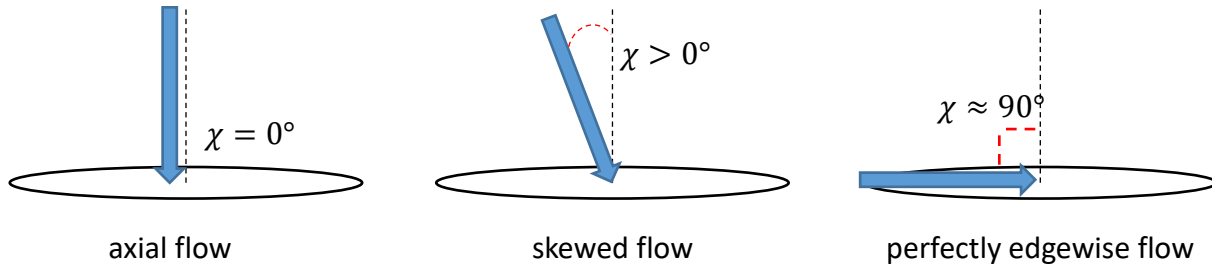


Figure 1.7. Axial, skewed, and perfectly edgewise flow figures.

With these three assumptions (an untrimmed rubber rotor with an infinite number of blades), Garcia-Duffy’s perfectly edgewise flow results exactly matched Glauert’s ideal induced power result.

$$\left(\frac{C_P}{C_T^2} \right)_{\text{Glauert}} = \left(\frac{C_P}{C_T^2} \right)_{\text{Duffy}(\chi \approx 90^\circ)} = \frac{1}{2\mu} \quad (1.3.1)$$

- Chad File (2013)

Chad File continued Garcia-Duffy's work and calculated the minimized induced power with an infinite number of blades but with more realistic than those used by Garcia-Duffy. File used conventional collective and cyclic pitch, higher harmonic controls, and the trimmed condition. Neither Garcia-Duffy nor File included reverse flow in their aerodynamics.

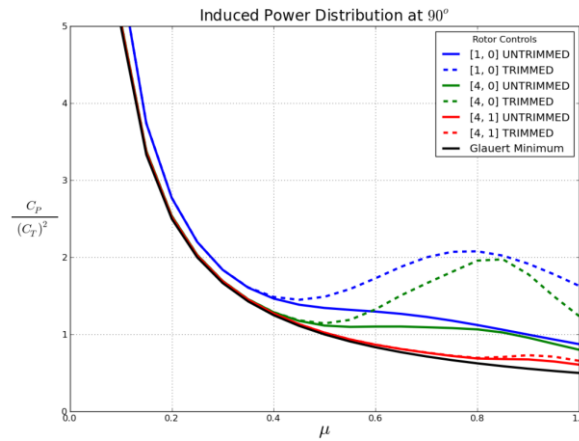


Figure 1.8. File's induced power results, Ref. [15].

Figure 1.8 shows induced power results with and without trim. In the plot legend, [1,0] represents conventional collective and cyclic pitch control; and any higher numbers within the brackets represent higher harmonic control. The induced power peaks near an advance ratio of 0.9 are not a surprise because Ormiston and Hall and Hall's results showed similar induced power peak behaviors.

Induced power approaches Glauert's minimum as the number of controls is increased, Fig. 1.8. It is interesting to see how both File and Hall and Hall produced results similar to Glauert's minimum by varying different parameters. File varied the number of controls with an infinite number of blades, and Hall and Hall varied the number of blades with an infinite number of

controls. As each approaches the condition of an infinite number of blades with infinite control, their respective induced power approach Galuert's minimum.

1.4 Present approach

This present work is continuation of the work of Duffy and File, Refs. [10] and [15]. Reverse-flow, inflow feedback, root-cutout, and a finite number of blades are added to File's model in order to obtain more realistic results for the minimum induced power. These refinements enable confirmation of the key results identified by Ormiston and Hall and Hall.

A quadratic optimization method is used herein, similar to that used by Garcia-Duffy and File, to compute the minimum induced power at a high advance ratio. Unlike these two predecessors, who performed optimization over a range of inflow skew angles, this dissertation focuses only on nearly perfectly edgewise flow ($\chi = 87.5^\circ$). This angle is chosen since it is nearly edgewise flow, but avoids the singularity at 90° . In this region, the effect of swirl velocity is small due to the high inflow skew angle conditions. Therefore, only the original form of the Peters-He finite-state inflow model is used.

In all previous applications of the Peters-He model, researchers and application specialists have used the model in the form of a real Fourier series around the azimuth (sine and cosine of ψ). In the present work, however, all cosines and sines are replaced with a complex exponential.

$$\begin{aligned}
\cos(m\psi) &\rightarrow \left(\frac{e^{im\psi} + e^{-im\psi}}{2} \right) \\
\sin(m\psi) &\rightarrow i \left(\frac{-e^{im\psi} + e^{-im\psi}}{2} \right)
\end{aligned} \tag{1.4.1}$$

Peters and He offered this exponential form in an internal Georgia Tech Research report, but never published it in the open literature. Many calculations become simpler when the Peters-He inflow model is represented in a complex exponential form.

To understand the limitation of modern rotors, the dissertation seeks to find the power of a rotor in flight at a high advance ratio under ideal conditions. The assumptions and approximations used in the work are as follows.

- 1) inviscid, incompressible, irrotational potential flow
- 2) rectangular blades
- 3) rigid blades (neglects the blade flapping motion)
- 4) airfoil with a linear lift curve (no stall and/or compressibility losses)
- 5) no propulsive force trim constraint
- 6) actuator disk model

The first assumption is valid because helicopter rotors typically operate at subsonic speeds with very high Reynolds numbers (of the order of one million). The second is quite reasonable because we are not designing the optimum blade – just the optimum lift distribution. Therefore, only a blade twist distribution is necessary. The third assumption is valid because even flapping blades ultimately reach a solution with a tip-path plane that can be considered an actuator disk without flapping. We used the forth assumption because we are seeking the ideal blade, against which other can compare rotors that do stall. The fifth assumption follows from the idea of high advance ratios. There, an external device is used for propulsive force so that the rotor is relieved of this task. The sixth assumption is valid because, even in hover, swirl is a small effect for lifting rotors. It follows that swirl is virtually eliminated at high advance ratios in edgewise flow.

2. Infinite Number of Blades

Induced flow theory with an infinite number of blades can be considered as a steady state theory. Therefore, the unsteady part of the inflow equations can be neglected when doing the analysis. Figure 2.1 shows the difference between the unsteady and steady parts of the dynamic wake model. The unsteady part will be added for a finite number of blades, later.

$$\begin{array}{c}
 \boxed{\begin{bmatrix} \ddots & & \\ & G_n^m & \\ & & \ddots \end{bmatrix} \begin{Bmatrix} \vdots \\ \dot{\gamma}_n^m \\ \vdots \end{Bmatrix}} + 2V[L] \begin{Bmatrix} \vdots \\ \gamma_n^m \\ \vdots \end{Bmatrix} = \begin{Bmatrix} \vdots \\ \tau_n^m \\ \vdots \end{Bmatrix} \\
 \text{Unsteady Part} \qquad \qquad \qquad \text{Steady Part}
 \end{array}$$

Figure 2.1. Unsteady and steady parts of the dynamic wake

2.1 Finite-State Inflow Theory

The following development generally follows Ref. [12]. As mentioned above, the steady part of the finite-state inflow theory will be used.

$$2V[L]\{\gamma_n^m\} = \{\tau_n^m\} \quad (2.1.1)$$

Peters and He developed complex version of [L] matrix and the definition is in Appendix E. According to the Peters/He theory, inflow and pressure distribution across the disk can be represented as inflow and pressure states, $\{\gamma\}$ and $\{\tau\}$, Ref. [12].

$$\omega(\bar{r}, \psi) = \sum_{r=-\infty}^{+\infty} \sum_{j=|r|+1, |r|+3, \dots}^{+\infty} \phi_j^r(\bar{r}) \gamma_j^r \cdot e^{ir\psi} \quad (2.1.2)$$

$$\Delta P(\bar{r}, \psi) = \sum_{m=-\infty}^{+\infty} \sum_{n=|m|+1, |m|+3, \dots}^{+\infty} \bar{P}_n^m(\nu) \tau_n^m \cdot e^{im\psi} \quad (2.1.3)$$

where ν is an ellipsoidal coordinate and has a relationship to the non-dimensional radius \bar{r} , given by

$$\nu = \sqrt{1 - \bar{r}^2} \quad (2.1.4)$$

The total number of states from the table method is $\frac{1}{2}*(M+1)(M+2)$, where M is the maximum harmonic used.

By moving variables from the left hand side to the right hand side of Eq. (2.1.1), the inflow state can be represented with pressure states as below.

$$\{\gamma_n^m\} = \left(\frac{1}{2V}\right) \cdot [L] \{\tau_n^m\} \quad (2.1.5)$$

2.2 Induced Power Formulation

Induced power can be computed by the inner product of the inflow and pressure distribution across the rotor disk area.

$$C_P = \frac{1}{\pi} \int_0^{2\pi} \int_0^1 w \cdot \Delta P \cdot \bar{r} \cdot d\bar{r} \cdot d\psi \quad (2.2.1)$$

Substitution of Eqs. (2.1.2) and (2.1.3) into Eq. (2.2.1) and solution of the double integral yields the compact induced power equation below.

$$C_P = 2 \sum_m \sum_n \{ \tau_n^{-m} \}^T \{ \gamma_n^m \} \quad (2.2.2)$$

Substitution of Eq. (2.1.5) to (2.2.2) yields:

$$\begin{aligned} C_P &= \left(\frac{1}{V} \right) \sum_m \sum_n \{ \tau_n^{-m} \}^T [L] \{ \tau_n^m \} \\ &= \left(\frac{1}{V} \right) \{ \tau \}^T [U] [L] \{ \tau \} \end{aligned} \quad (2.2.3)$$

where $[U]$ is used to flip the order of $\{ \tau_n^{-m} \}$ so that $\{ \tau_n^{-m} \}^T = \{ \tau_n^m \}^T [U]$. Note that this complex form of the equation differs from Ref. [15] by a factor of 2.

Mass flow, V , is approximately equal to the advance ratio, μ , in high-speed forward flight with a skew angle close to 90° . $[L]$ depends only on the skew angle. Therefore, Eq. (2.2.3) shows that the pressure states, $\{ \tau \}$, are the only information required to calculate the induced power.

2.3 Rotor Loads in Terms of Pressure Expansions

The complete set of trim loads includes all six integrated rotor aerodynamic forces and moments on the fuselage: thrust, roll moment, pitch moment, yaw moment, side force, and drag. In this dissertation, we concentrate on the first three loads, because the other three loads are not balanced by the rotor itself. Thrust, roll moment, and pitch moment can be represented by pressure states, as below.

$$\begin{aligned} C_T &= \frac{1}{\pi} \int_0^{2\pi} \int_0^1 \Delta P \cdot \bar{r} \cdot d\bar{r} \cdot d\psi \\ C_L &= -\frac{1}{\pi} \int_0^{2\pi} \int_0^1 \Delta P \cdot (\bar{r} \cdot \sin(\psi)) \cdot \bar{r} \cdot d\bar{r} \cdot d\psi \\ C_M &= -\frac{1}{\pi} \int_0^{2\pi} \int_0^1 \Delta P \cdot (\bar{r} \cdot \cos(\psi)) \cdot \bar{r} \cdot d\bar{r} \cdot d\psi \end{aligned} \quad (2.3.1)$$

Substitution of the pressure difference in Eq. (2.1.3) into (2.3.1) and solving the double integral yields

$$\{C\} = [D]\{\tau\} \quad (2.3.2)$$

where $\{C\}$ is the column of C_T , C_L , and C_M , and $\{\tau\}$ is the column of τ_2^{-1} , τ_1^0 , τ_2^1 , and where

$$[D] = \begin{bmatrix} \dots & 0 & \dots & \frac{2}{\sqrt{3}} & \dots & 0 & \dots \\ \dots & i\sqrt{\frac{2}{15}} & \dots & 0 & \dots & -i\sqrt{\frac{2}{15}} & \dots \\ \dots & -\sqrt{\frac{2}{15}} & \dots & 0 & \dots & -\sqrt{\frac{2}{15}} & \dots \end{bmatrix} \quad (2.3.3)$$

The analysis above assumes that the lift vector is perpendicular to the rotor disk plane rather than to the local air velocity vector. This is a reasonable assumption because a skew angle close to 90° makes the effect of the lift vector tilt negligible.

2.4 Blade Pitch Angle in Terms of Rotor Control

Either higher-harmonic control or radial rotor control allows the lift distribution along the blade to be altered as a function of azimuth. More control means having more ability to tailor the lift distribution into the ideal shape. Theoretically, having an infinite amount of control and having an infinite number of blades can reduce the induced power to Glauert's ideal power. Hall and Hall used infinite control (a rubber blade) in Ref. [4] and showed that the computed induced power approached Glauert's ideal power as the number of blades was increased. Typical examples of realistic rotor control are collective and cyclic pitch, higher harmonic control, blade twist, variable airfoil geometry, and even circulation control through local blowing.

For this dissertation, we assume the rotor control vector $\{\theta\}$ to be of the following form, which can cover all the existing conventional and innovative approaches.

$$\theta(\bar{r}, \psi) = \sum_{h=-H}^H \sum_{d=0}^D \bar{r}^d \cdot \theta_d^h e^{ih\psi} \quad (2.4.1)$$

Many rotor controls are possible with this form. Conventional collective and cyclic pitch control ($H = 1, D = 0$) is used as the minimum control input in this present paper. Higher harmonic control results ($H > 1, D > 0$) will also be discussed in the Results section.

2.5 Blade Element Lift in Terms of Rotor Pitch and Inflow

According to conventional blade-element theory, the rotor blade airfoil sectional lift per unit length may be expressed in terms of the section velocity components, U_P and U_T .

$$L_q = \left(\frac{1}{2}\right) \rho a c \left[U_T^2 \cdot \theta - U_P \cdot U_T \right] \quad (2.5.1)$$

where U_T and U_P are

$$\begin{aligned} U_T &= \Omega R (\bar{r} + \mu \cdot \sin(\psi)) \\ U_P &= \Omega R (\lambda + w(\bar{r}, \psi)) \end{aligned} \quad (2.5.2)$$

Note that for the present purpose of rotor performance analysis, rotor blade flapping motion is not included. In this dissertation, it is assumed that the lift curve slope, a , has a constant value, 6.0, with the assumption that the blade does not stall. Equations (2.5.1) and (2.5.2) show that induced inflow, $w(\bar{r}, \psi)$, changes the lift distribution, which consequently changes the induced power. Previous studies by File neglected the effect of inflow feedback in Refs. [14] and [15].

2.6 Pressure Expansions in Terms of Rotor Control and Inflow Feedback

The relationship between pressure and blade sectional lift can be founded in Ref. [12].

Changing this relationship into a complex form yields

$$\{\tau\} = \frac{1}{2\pi} \sum_{q=1}^Q \int_{rco}^1 \frac{L_q}{\rho \Omega^2 R^3} \cdot \phi_n^m(\bar{r}) \cdot d\bar{r} \cdot e^{-im\psi} \quad (2.6.1)$$

$$L = \text{total Lift} = L_q \cdot Q \quad (2.6.2)$$

$$d\psi = \frac{2\pi}{Q} \quad \rightarrow \quad \frac{1}{Q} = \frac{d\psi}{2\pi} \quad \text{and} \quad \sum_{q=1}^Q \quad \rightarrow \quad \int_0^{2\pi} \quad (2.6.3)$$

Substituting total lift into Eq. (2.6.1), and changing the summation sign to an integral sign yields

$$\tau_n^m = \left(\frac{\sigma a}{4} \right) \cdot \left(\frac{1}{2\pi} \right) \cdot \left(\int_0^{2\pi} \int_{rco}^1 (\bar{r} + \mu \sin(\psi))^2 [\theta(\bar{r}, \psi)] (\phi_n^m) \cdot e^{-im\psi} \cdot d\bar{r} \cdot d\psi \right. \\ \left. - \int_0^{2\pi} \int_{rco}^1 (\bar{r} + \mu \sin(\psi)) (\lambda + w(\bar{r}, \psi)) (\phi_n^m) \cdot e^{-im\psi} \cdot d\bar{r} \cdot d\psi \right) \quad (2.6.4)$$

Changing the sine and cosine into their complex forms, followed by substitution of the pitch angle and induced inflow distribution (Eqs. (2.4.1) and (2.1.2)) into Eq. (2.6.4), yields

$$\{\tau\} = \frac{\sigma a}{4} \cdot \left[[A]\{\theta\} - [B]\{\gamma\} \right] \quad (2.6.5)$$

where

$$\{\theta\} = \left\{ \begin{array}{c} \vdots \\ \theta_d^h \\ \vdots \end{array} \right\} \quad (2.6.6)$$

Equation (2.6.5) involves pressure expansions, rotor controls, and inflow feedback. The term $[B]\{\gamma\}$ is the inflow feedback, since $\{\tau\}$ which derives $\{\gamma\}$ now becomes a function of $\{\gamma\}$. In order to solve for $\{\gamma\}$ in terms of $\{\tau\}$, we need to substitute Eq. (2.1.5) into equation (2.6.5). With the simplification process described in Appendix C, Eq. (2.6.5) can be transformed into the equation below.

$$\begin{aligned}\{\tau\} &= \frac{\sigma a}{4} \cdot \left[[I] + \frac{\sigma a}{8V} [B][L] \right]^{-1} [A] \{\theta\} \\ &= [P] \{\theta\}\end{aligned}\tag{2.6.7}$$

where

$$[P] = \frac{\sigma a}{4} \cdot \left[[I] + \frac{\sigma a}{8V} [B][L] \right]^{-1} [A]\tag{2.6.8}$$

$[A]$ and $[B]$ can be expanded as below.

$$\begin{aligned}[A] &= \frac{1}{2\pi} \cdot \int_0^{2\pi} \int_{rco}^1 \bar{r}^d \cdot (\bar{r} + \mu \cdot \sin(\psi))^2 \cdot \phi_n^m \cdot e^{i\psi(h-m)} \cdot d\bar{r} \cdot d\psi \\ [B] &= \frac{1}{2\pi} \cdot \int_0^{2\pi} \int_{rco}^1 (\bar{r} + \mu \cdot \sin(\psi)) \cdot \phi_n^m \cdot \phi_j^r \cdot e^{i\psi(r-m)} \cdot d\bar{r} \cdot d\psi\end{aligned}\tag{2.6.9}$$

$$\begin{aligned}\therefore [A] &= \frac{1}{2\pi} \cdot \left(\left[\int_{rco}^1 \bar{r}^{(2+d)} \cdot \phi_n^m \cdot d\bar{r} \right] \cdot \left[\int_0^{2\pi} e^{i\psi(h-m)} \cdot d\psi \right] \right. \\ &\quad \left. + (i) \cdot \mu \cdot \left[\int_{rco}^1 \bar{r}^{(1+d)} \cdot \phi_n^m \cdot d\bar{r} \right] \cdot \left[\int_0^{2\pi} -e^{i\psi(h-m+1)} + e^{i\psi(h-m-1)} \cdot d\psi \right] \right. \\ &\quad \left. + \left(-\frac{1}{4} \right) \cdot \mu^2 \cdot \left[\int_{rco}^1 \bar{r}^d \cdot \phi_n^m \cdot d\bar{r} \right] \cdot \left[\int_0^{2\pi} e^{i\psi(h-m+2)} - 2e^{i\psi(h-m)} + e^{i\psi(h-m-2)} \cdot d\psi \right] \right)\end{aligned}\tag{2.6.10}$$

$$\begin{aligned}\therefore [B] &= \frac{1}{2\pi} \cdot \left(\left[\int_{rco}^1 \bar{r} \cdot \phi_n^m \cdot \phi_j^r \cdot d\bar{r} \right] \cdot \left[\int_0^{2\pi} e^{i\psi(r-m)} \cdot d\psi \right] \right. \\ &\quad \left. + \left(\frac{1}{2} \right) \cdot (i) \cdot \mu \cdot \left[\int_{rco}^1 \phi_n^m \cdot \phi_j^r \cdot d\bar{r} \right] \cdot \left[\int_0^{2\pi} -e^{i\psi(r-m+1)} + e^{i\psi(r-m-1)} \cdot d\psi \right] \right)\end{aligned}\tag{2.6.11}$$

Note that the effect of induced inflow feedback, $[B]$, is multiplied by a factor of $\frac{\sigma a}{8V}$. For a given value of the lift curve slope, a , and mass flow, V , solidity, σ , is the only parameter that determines the magnitude of the inflow feedback.

2.7 Reverse Flow

Helicopters in high speed flight (i.e., at a high advance ratio) experience reverse flow over a significant part of the blade when the advance ratio is higher than the root-cutout value. Reverse flow is defined as the condition in which the free-stream velocity impacts the trailing edge of the blade rather than the leading edge. This condition occurs because blade sections in the retreating side are traveling slower than the free stream velocity.

Reverse flow makes the traditional lift formula in Eq. (2.5.1) incorrect, because it assumes flow is impacting the leading edge. As a result, lift in a reverse flow has an opposite sign predicted by Eq. (2.5.1). In order to account for this lift reversal in reverse flow, Eq. (2.5.1) must be modified to include an absolute value sign on the tangential velocity.

$$\begin{aligned}
 \text{Original (2.5.1)} \quad L_q &= \left(\frac{1}{2}\right) \rho a c \left[U_T^2 \cdot \theta - U_P \cdot U_T \right] \\
 \text{Modified (2.5.1)} \quad L_q &= \left(\frac{1}{2}\right) \rho a c \left[U_T \cdot |U_T| \cdot \theta - U_P \cdot |U_T| \right]
 \end{aligned} \tag{2.7.1}$$

where

$$U_T = \Omega R (\bar{r} + \mu \cdot \sin(\psi)) \tag{2.7.2}$$

Tangential velocity, sectional lift, and pressure distribution become negative when \bar{r} is small and $\mu \cdot \sin(\psi)$ is big enough. This absolute value complicates the integrals of lift required for thrust, pitching moment, rolling moment, and power. There are two ways to calculate the pressure distribution with reverse flow lift reversal.

One way to calculate the $[A]$ and $[B]$ matrixes is numerical evaluation of the double integrals with the absolute value sign (since there is no closed form integrand in this case). This implies numerical quadrature of $d\bar{r}$ and $d\psi$.

$$\begin{aligned}
[A]_{\text{combined}} &= \frac{1}{2\pi} \cdot \int_0^{2\pi} \int_{rco}^1 \bar{r}^d \cdot (\bar{r} + \mu \cdot \sin(\psi)) \cdot |\bar{r} + \mu \cdot \sin(\psi)| \cdot \phi_n^m \cdot e^{i\psi(h-m)} \cdot d\bar{r} \cdot d\psi \\
[B]_{\text{combined}} &= \frac{1}{2\pi} \cdot \int_0^{2\pi} \int_{rco}^1 |\bar{r} + \mu \cdot \sin(\psi)| \cdot \phi_n^m \cdot \phi_j^r \cdot e^{i\psi(r-m)} \cdot d\bar{r} \cdot d\psi
\end{aligned} \tag{2.7.3}$$

Another way to calculate the $[A]$ and $[B]$ matrixes is to break the integral into two parts, thus eliminating the explicit absolute value sign from the expressions.

$$\begin{aligned}
[A]_{\text{combined}} &= [A] - 2 \cdot [A]_{\text{Rev}} \\
[B]_{\text{combined}} &= [B] - 2 \cdot [B]_{\text{Rev}}
\end{aligned} \tag{2.7.4}$$

$$[A]_{\text{Rev}} \text{ and } [B]_{\text{Rev}} \text{ exist only when } \mu > rco \tag{2.7.5}$$

$$\begin{aligned}
\therefore [A]_{\text{Rev}} &= \\
&\frac{1}{2\pi} \cdot \left(\left[\int_{rco}^{\bar{r}_{rev}} \bar{r}^{(2+d)} \cdot \phi_n^m \cdot d\bar{r} \right] \cdot \left[\int_{\psi_1}^{\psi_2} e^{i\psi(h-m)} \cdot d\psi \right] \right. \\
&\quad + (i) \cdot \mu \cdot \left[\int_{rco}^{\bar{r}_{rev}} \bar{r}^{(1+d)} \cdot \phi_n^m \cdot d\bar{r} \right] \cdot \left[\int_{\psi_1}^{\psi_2} -e^{i\psi(h-m+1)} + e^{i\psi(h-m-1)} \cdot d\psi \right] \\
&\quad \left. + \left(-\frac{1}{4} \right) \cdot \mu^2 \cdot \left[\int_{rco}^{\bar{r}_{rev}} \bar{r}^d \cdot \phi_n^m \cdot d\bar{r} \right] \cdot \left[\int_{\psi_1}^{\psi_2} e^{i\psi(h-m+2)} - 2e^{i\psi(h-m)} + e^{i\psi(h-m-2)} \cdot d\psi \right] \right)
\end{aligned} \tag{2.7.6}$$

$$\begin{aligned}
\therefore [B]_{\text{Rev}} &= \frac{1}{2\pi} \cdot \left(\left[\int_{rco}^{\bar{r}_{rev}} \bar{r} \cdot \phi_n^m \cdot \phi_j^r \cdot d\bar{r} \right] \cdot \left[\int_{\psi_1}^{\psi_2} e^{i\psi(r-m)} \cdot d\psi \right] \right. \\
&\quad \left. + \left(\frac{1}{2} \right) \cdot (i) \cdot \mu \cdot \left[\int_{rco}^{\bar{r}_{rev}} \phi_n^m \cdot \phi_j^r \cdot d\bar{r} \right] \cdot \left[\int_{\psi_1}^{\psi_2} -e^{i\psi(r-m+1)} + e^{i\psi(r-m-1)} \cdot d\psi \right] \right)
\end{aligned} \tag{2.7.7}$$

$$\bar{r}_{rev} = \begin{cases} \mu & \text{if } \mu \leq 1 \\ 1 & \text{if } \mu > 1 \end{cases} \tag{2.7.8}$$

$$\begin{aligned}
\psi_2 &= 2\pi - \sin^{-1} \left(\bar{r} / \mu \right) \\
\psi_1 &= \sin^{-1} \left(\bar{r} / \mu \right) + \pi
\end{aligned} \tag{2.7.9}$$

When the integral is broken up in this way, the $d\psi$ integral can be done in closed form, thus leaving only a $d\bar{r}$ integral to be performed numerically. The first method may appear to be simpler

in concept than the second method. However, for the same level of accuracy, the second method saves considerable amount of computational time.

3. Finite Number of Blades

When a finite number of blades is included in the induced flow theory, the equations become time varying, i.e., pressure and inflow distributions vary with time. Therefore, the entire form of the dynamic wake model will be used.

$$\left[\begin{array}{ccc} \ddots & & \\ & G_n^m & \\ & & \ddots \end{array} \right] \left\{ \begin{array}{c} \vdots \\ \dot{\gamma}_n^m \\ \vdots \end{array} \right\} + 2V[L] \left\{ \begin{array}{c} \vdots \\ \gamma_n^m \\ \vdots \end{array} \right\} = \left\{ \begin{array}{c} \vdots \\ \tau_n^m \\ \vdots \end{array} \right\}$$

Figure 3.1. Unsteady form of dynamic wake model.

This unsteady model is solved in the frequency domain for the induced flow, and then the same processes from 2.3 – 2.5 can be used in the blade element theory. We begin with the harmonic balance solution.

3.1 Finite-State Inflow Theory

The following development generally follows Ref. [2].

$$\left[G_n^m \right] \left\{ \dot{\gamma}_n^m \right\} + 2V[L] \left\{ \gamma_n^m \right\} = \left\{ \tau_n^m \right\} \quad (3.1.1)$$

Because the above inflow equation is an ordinary differential equation in time (non-dimensional), it must be solved for the steady state. One method would be to time march until all transient decay, but we are looking for a closed-form solution. To do that, we use a complex harmonic balance in terms of $\{\tau\}_k$ and $\{\gamma\}_\ell$:

$$\{\tau\} = \sum_k \{\tau\}_k e^{ikt}, \quad \{\gamma\} = \sum_\ell \{\gamma\}_\ell e^{i\ell t} \quad (3.1.2)$$

It follows that the resultant induced flow field becomes a function of non-dimensional radius, azimuth, and time.

$$\omega(\bar{r}, \psi, t) = \sum_{\ell=-\infty}^{+\infty} \sum_{r=-\infty}^{+\infty} \sum_{j=|r|+1, |r|+3, \dots}^{+\infty} \phi_j^r(\bar{r}) \{\gamma_j^r\}_\ell \cdot e^{ir\psi} \cdot e^{i\ell t} \quad (3.1.3)$$

$$\Delta P(\bar{r}, \psi, t) = \sum_{k=-\infty}^{+\infty} \sum_{m=-\infty}^{+\infty} \sum_{n=|m|+1, |m|+3, \dots}^{+\infty} \bar{P}_n^m(\nu) \{\tau_n^m\}_k \cdot e^{im\psi} \cdot e^{ikt} \quad (3.1.4)$$

Once the Fourier series is substituted into Eq. (3.1.1), we collect like harmonics and form a set of linear algebraic equations for the harmonics of the inflow states.

$$\{\gamma_n^m\}_k = \left(1/2V\right) \cdot [R]_k \{\tau_n^m\}_k \cdot e^{ikt} \quad (3.1.5)$$

where

$$[R]_k = \left[\frac{ik}{2V} [G] + [L]^{-1} \right]^{-1} \quad (3.1.6)$$

3.2 Induced Power Formulation

Induced power is computed by the dot product of the inflow and pressure across the rotor disk.

$$C_P = \frac{1}{2\pi} \cdot \int_0^{2\pi} \frac{1}{\pi} \int_0^{2\pi} \int_0^1 w \cdot \Delta P \cdot \bar{r} \cdot d\bar{r} \cdot d\psi \cdot dt \quad (3.2.1)$$

Substitution of Eqs. (3.1.2) and (3.1.3) into Eq. (3.2.1) results in a double integral for the power.

Due to the orthogonality of the expansion functions in Eqs. (3.1.2) and (3.1.3), a compact induced power equation is obtained:

$$C_P = 2 \sum_k \sum_m \sum_n \left\{ \tau_n^{-m} \right\}_{-k}^T \left\{ \gamma_n^m \right\}_k \quad (3.2.2)$$

Substitution of Eq. (3.1.4) into (3.2.2) yields

$$\begin{aligned} C_P &= \left(\frac{1}{V} \right) \sum_k \sum_m \sum_n \left\{ \tau_n^{-m} \right\}_{-k}^T [R]_k \left\{ \tau_n^m \right\}_k \\ &= \left(\frac{1}{V} \right) \left\{ \tau \right\}_{-k}^T [U][R]_k \left\{ \tau \right\}_k \end{aligned} \quad (3.2.3)$$

Equation (3.2.3) shows that the pressure states, $\{\tau\}_k$, are the only information required to calculate the induced power.

3.3 Pressure Expansions in Terms of Rotor Control with Inflow Feedback

The relationship between pressure and blade sectional lift for a finite number of blades starts from Eq. (2.6.1), which can be re-written as

$$\left\{ \tau \right\} = \frac{1}{2\pi} \sum_{q=1}^Q \int_{rco}^1 \frac{L_q}{\rho \Omega^2 R^3} \cdot \phi_n^m(\bar{r}) \cdot d\bar{r} \cdot e^{-im\psi} \quad (3.3.1)$$

$$L = \text{total Lift} = L_q \cdot Q \quad (3.3.2)$$

In chapter 2.6, this integral was taken respect to azimuth for an infinite number of blades. In contrast, the integral is now taken with respect to non-dimensional time for a finite number of blades.

$$\left\{ \tau_n^m \right\}_k = \frac{1}{2\pi} \int_0^{2\pi} \left(\frac{1}{2\pi} \cdot \frac{1}{Q} \sum_{q=1}^Q \int_{rco}^1 \frac{L}{\rho \Omega^2 R^3} \phi_n^m d\bar{r} \cdot e^{-im\psi_q} \cdot e^{-ikt} \right) \cdot dt \quad (3.3.3)$$

The multi-blade identities allow the ψ_q terms to be written in terms of t , and the only surviving terms are integer multiples of the blade number.

$$\text{Multi-Blade Identities} \Rightarrow \frac{1}{Q} \sum_{q=1}^Q e^{k_{\psi q}} = \begin{cases} 0 & k \neq \text{integer multiple of } Q \\ e^{kt} & k = 0, \pm Q, \pm 2Q, \dots \end{cases} \quad (3.3.4)$$

$$\{\tau_n^m\}_k = \frac{1}{2\pi} \int_0^{2\pi} \frac{1}{2\pi} \int_{rco}^1 \frac{L}{\rho \Omega^2 R^3} \phi_n^m \cdot e^{-imt} \cdot e^{-ikt} \cdot d\bar{r} \cdot dt \quad (3.3.5)$$

Substitution of the total lift into Eq. (3.3.5), followed by simplification, yields a similar equation to that obtained from the analysis with an infinite number of blades.

$$\begin{aligned} \{\bar{\tau}\} &= \frac{\sigma a}{4} \cdot \left[[\bar{I}] + \frac{\sigma a}{8V} [\bar{B}] [\bar{R}] \right]^{-1} [\bar{A}] \{\theta\} \\ &= [\bar{P}] \{\theta\} \end{aligned} \quad (3.3.6)$$

where

$$[\bar{P}] = \frac{\sigma a}{4} \cdot \left[[\bar{I}] + \frac{\sigma a}{8V} [\bar{B}] [\bar{R}] \right]^{-1} [\bar{A}] \quad (3.3.7)$$

The relationships between a bar matrix, $[\bar{\quad}]$, and a normal matrix $[\quad]$ are given by

$$\{\bar{\tau}\} = \begin{bmatrix} \vdots \\ \{\tau\}_{-2Q} \\ \{\tau\}_{-Q} \\ \{\tau\}_0 \\ \{\tau\}_Q \\ \{\tau\}_{2Q} \\ \vdots \end{bmatrix} \quad [\bar{P}] = \begin{bmatrix} \vdots \\ [P]_{-2Q} \\ [P]_{-Q} \\ [P]_0 \\ [P]_Q \\ [P]_{2Q} \\ \vdots \end{bmatrix} \quad [\bar{A}] = \begin{bmatrix} \vdots \\ [A]_{-2Q} \\ [A]_{-Q} \\ [A]_0 \\ [A]_Q \\ [A]_{2Q} \\ \vdots \end{bmatrix} \quad (3.3.8)$$

$$[\bar{I}] = \begin{bmatrix} \ddots & & & & & \\ & [I] & & & & \\ & & [I] & & & \\ & & & [I] & & \\ & & & & [I] & \\ & & & & & [I] \\ & & & & & & \ddots \end{bmatrix} \quad [\bar{R}] = \begin{bmatrix} \ddots & & & & & \\ & [R]_{-2Q} & & & & \\ & & [R]_{-Q} & & & \\ & & & [R]_0 & & \\ & & & & [R]_Q & \\ & & & & & [R]_{2Q} \\ & & & & & & \ddots \end{bmatrix} \quad (3.3.9)$$

Two examples are used to illustrate the $[\bar{B}]$ matrix, which can be difficult to visualize

Example 1) M=6, Q=3

$$[\bar{B}] = \begin{bmatrix} [B]_0 & [B]_{-3} & [B]_{-6} & & \\ [B]_3 & [B]_0 & [B]_{-3} & [B]_{-6} & \\ [B]_6 & [B]_3 & [B]_0 & [B]_{-3} & [B]_{-6} \\ & [B]_6 & [B]_3 & [B]_0 & [B]_{-3} \\ & & [B]_6 & [B]_3 & [B]_0 \end{bmatrix} \quad (3.3.10)$$

Example 2) M=12, Q=4

$$[\bar{B}] = \begin{bmatrix} [B]_0 & [B]_{-4} & [B]_{-8} & [B]_{-12} & & & \\ [B]_4 & [B]_0 & [B]_{-4} & [B]_{-8} & [B]_{-12} & & \\ [B]_8 & [B]_4 & [B]_0 & [B]_{-4} & [B]_{-8} & [B]_{-12} & \\ [B]_{12} & [B]_8 & [B]_4 & [B]_0 & [B]_{-4} & [B]_{-8} & [B]_{-12} \\ & [B]_{12} & [B]_8 & [B]_4 & [B]_0 & [B]_{-4} & [B]_{-8} \\ & & [B]_{12} & [B]_8 & [B]_4 & [B]_0 & [B]_{-4} \\ & & & [B]_{12} & [B]_8 & [B]_4 & [B]_0 \end{bmatrix} \quad (3.3.11)$$

$[A]_k$ and $[B]_{(k-l)}$ can be expanded as below.

$$\begin{aligned} \therefore [A]_k = & \frac{1}{2\pi} \cdot \left(\left[\int_{rco}^1 \bar{r}^{(2+d)} \cdot \left(J_0 \left(m\bar{b}/\bar{r} \right) \right) \cdot \phi_n^m \cdot dr \right] \cdot \left[\int_0^{2\pi} \left[e^{it(h-m)} \right] \cdot \left[e^{-ikt} \right] \cdot dt \right] \right. \\ & + (i) \cdot \mu \cdot \left[\int_{rco}^1 \bar{r}^{(1+d)} \cdot \left(J_0 \left(m\bar{b}/\bar{r} \right) \right) \cdot \phi_n^m \cdot d\bar{r} \right] \cdot \left[\int_0^{2\pi} \left[-e^{it(h-m+1)} + e^{it(h-m-1)} \right] \cdot \left[e^{-ikt} \right] \cdot dt \right] \\ & \left. + \left(-\frac{1}{4} \right) \cdot \mu^2 \cdot \left[\int_{rco}^1 \bar{r}^d \cdot \left(J_0 \left(m\bar{b}/\bar{r} \right) \right) \cdot \phi_n^m \cdot d\bar{r} \right] \cdot \left[\int_0^{2\pi} \left[e^{it(h-m+2)} - 2e^{it(h-m)} + e^{it(h-m-2)} \right] \cdot \left[e^{-ikt} \right] \cdot dt \right] \right) \end{aligned} \quad (3.3.12)$$

$$\begin{aligned} \therefore [B]_{(k-l)} = & \frac{1}{2\pi} \cdot \left(\left[\int_{rco}^1 \bar{r} \cdot \left(J_0 \left(m\bar{b}/\bar{r} \right) \right) \cdot \left(J_0 \left(r\bar{b}/\bar{r} \right) \right) \cdot \phi_n^m \cdot \phi_j^r \cdot d\bar{r} \right] \cdot \left[\int_0^{2\pi} \left[e^{it(r-m)} \right] \cdot \left[e^{-it(k-l)} \right] \cdot dt \right] \right. \\ & \left. + \left(\frac{1}{2} \right) \cdot (i) \cdot \mu \cdot \left[\int_{rco}^1 \left(J_0 \left(m\bar{b}/\bar{r} \right) \right) \cdot \left(J_0 \left(r\bar{b}/\bar{r} \right) \right) \cdot \phi_n^m \cdot \phi_j^r \cdot d\bar{r} \right] \cdot \left[\int_0^{2\pi} \left[-e^{it(r-m+1)} + e^{it(r-m-1)} \right] \cdot \left[e^{-it(k-l)} \right] \cdot dt \right] \right) \end{aligned} \quad (3.3.13)$$

3.4 Reverse Flow with a Finite Number of Blades

Two choices are available for adding reverse flow effect with a finite number of blades.

1. Perform a numerical double integral in $d\psi$ and $d\bar{r}$ with the absolute value sign.
2. Break up the integral into two parts to remove the absolute value sign, which makes one integral in closed form, leaving only the $d\bar{r}$ integral to be performed numerically.

The second method is chosen in order to save computational time.

$$\begin{aligned} [A]_{k_combined} &= [A]_k - 2 \cdot [A]_{k_Rev} \\ [B]_{(k-l)_combined} &= [B]_{(k-l)} - 2 \cdot [B]_{(k-l)_Rev} \end{aligned} \quad (3.4.1)$$

$$[A]_{Rev} \text{ and } [B]_{Rev} \text{ exist only when } \mu > rco \quad (3.4.2)$$

$$\begin{aligned} \therefore [A]_{k_Rev} = & \frac{1}{2\pi} \cdot \left(\left[\int_{rco}^{\bar{r}_{rev}} \bar{r}^{(2+p)} \cdot \left(J_0 \left(m\bar{b}/\bar{r} \right) \right) \cdot \phi_n^m \cdot dr \right] \cdot \left[\int_{\psi_1}^{\psi_2} \left[e^{i\psi(h-m)} \right] \cdot \left[e^{-ik\psi} \right] \cdot d\psi \right] \right. \\ & + (i) \cdot \mu \cdot \left[\int_{rco}^{\bar{r}_{rev}} \bar{r}^{(1+p)} \cdot \left(J_0 \left(m\bar{b}/\bar{r} \right) \right) \cdot \phi_n^m \cdot dr \right] \cdot \left[\int_{\psi_1}^{\psi_2} \left[-e^{i\psi(h-m+1)} + e^{i\psi(h-m-1)} \right] \cdot \left[e^{-ik\psi} \right] \cdot d\psi \right] \\ & \left. + \left(-\frac{1}{4} \right) \cdot \mu^2 \cdot \left[\int_{rco}^{\bar{r}_{rev}} \bar{r}^p \cdot \left(J_0 \left(m\bar{b}/\bar{r} \right) \right) \cdot \phi_n^m \cdot dr \right] \cdot \left[\int_{\psi_1}^{\psi_2} \left[e^{i\psi(h-m+2)} - 2e^{i\psi(h-m)} + e^{i\psi(h-m-2)} \right] \cdot \left[e^{-ik\psi} \right] \cdot d\psi \right] \right) \end{aligned} \quad (3.4.3)$$

$$\begin{aligned} \therefore [B]_{(k-\ell)\text{-Rev}} &= 1/2\pi \cdot \\ &\left(\left[\int_{rco}^{\bar{r}_{rev}} \bar{r} \cdot \left(J_0 \left(m\bar{b}/\bar{r} \right) \right) \cdot \left(J_0 \left(r\bar{b}/\bar{r} \right) \right) \cdot \phi_n^m \cdot \phi_j^r \cdot d\bar{r} \right] \cdot \left[\int_{\psi_1}^{\psi_2} \left[e^{i\psi(r-m)} \right] \cdot \left[e^{-i\psi(k-\ell)} \right] \cdot d\psi \right] \right. \\ &\quad \left. + \left(\frac{1}{2} \right) \cdot (i) \cdot \mu \cdot \left[\int_{rco}^{\bar{r}_{rev}} \left(J_0 \left(m\bar{b}/\bar{r} \right) \right) \cdot \left(J_0 \left(r\bar{b}/\bar{r} \right) \right) \cdot \phi_n^m \cdot \phi_j^r \cdot d\bar{r} \right] \cdot \left[\int_{\psi_1}^{\psi_2} \left[-e^{i\psi(r-m+1)} + e^{i\psi(r-m-1)} \right] \cdot \left[e^{-i\psi(k-\ell)} \right] \cdot d\psi \right] \right) \end{aligned} \quad (3.4.4)$$

$$\bar{r}_{rev} = \begin{cases} \mu & \text{if } \mu \leq 1 \\ 1 & \text{if } \mu > 1 \end{cases} \quad (3.4.5)$$

$$\begin{aligned} \psi_2 &= 2\pi - \sin^{-1} \left(\bar{r}/\mu \right) \\ \psi_1 &= \sin^{-1} \left(\bar{r}/\mu \right) + \pi \end{aligned} \quad (3.4.6)$$

4. Optimization

4.1 Infinite Number of Blades

Optimum performance for a helicopter rotor is typically defined for a specified trim condition; in the present work, this generally means a given thrust with zero pitching and rolling moment values. These conditions are used as constraints for the induced power optimization.

The optimization procedure starts with the definition of a functional, $F(\tau)$, in terms of the induced power coefficient, C_p , with the loading constraints, $\{C\}$, and Lagrange multipliers, $\{\Lambda\}$.

$$F(\tau) = C_p - \{C\}^T \{\Lambda\} \quad (4.1.1)$$

Substitution of Eqs. (2.3.2) and (2.2.3) into Eq. (2.6.5) yields

$$\begin{aligned} F(\tau) &= \frac{1}{V} \{\tau\}^T [U][L]\{\tau\} - \{\tau\}^T \{D\}^T \{\Lambda\} \\ &= \frac{1}{V} \{\theta\}^T [P]^T [U]^T [L][P]\{\theta\} - \{\theta\}^T [P]^T \{D\}^T \{\Lambda\} \end{aligned} \quad (4.1.2)$$

For simplicity, we define the following grouping by $[X]$.

$$[X] = [P]^T [U]^T [L][P] \quad (4.1.3)$$

Taking the variation with respect to $F(\theta)$ and setting it equal to zero will give the optimality condition for C_p .

$$\begin{aligned}
\delta F(\theta) &= \frac{1}{V} \{\delta\theta\}^T [X] \{\theta\} + \frac{1}{V} \{\theta\}^T [X] \{\delta\theta\} - \{\delta\theta\}^T [P]^T [D]^T \{\Lambda\} \\
&= \frac{1}{V} \{\delta\theta\}^T [X] \{\theta\} + \frac{1}{V} \{\delta\theta\}^T [X]^T \{\theta\} - \{\delta\theta\}^T [\bar{P}]^T [D]^T \{\Lambda\} \\
&= \frac{2}{V} \{\delta\theta\}^T \left(\frac{[X] + [X]^T}{2} \right) \{\theta\} - \{\delta\theta\}^T [\bar{P}]^T [D]^T \{\Lambda\} \\
&= \frac{2}{V} \{\delta\theta\}^T [X]_{sym} \{\theta\} - \{\delta\theta\}^T [P]^T [D]^T \{\Lambda\}
\end{aligned} \tag{4.1.4}$$

where $[X]_{sym}$ is the symmetric part of $[X]$.

Optimum controls can be found from the above equation:

$$\{\theta\} = \frac{V}{2} [X_{sym}]^{-1} [P]^T [D]^T \{\Lambda\} \tag{4.1.5}$$

The Lagrange multiplier can be found from Eq. (4.1.5)

$$\{\Lambda\} = \frac{2}{V} \left([D][P][X_{sym}]^{-1} [P]^T [D]^T \right)^{-1} \{C\} \tag{4.1.6}$$

Substitution of the Lagrange multiplier into (3.5) yields

$$\{\theta\} = [X_{sym}]^{-1} [P]^T [D]^T \left([D][P][X_{sym}]^{-1} [P]^T [D]^T \right)^{-1} \{C\} \tag{4.1.7}$$

Equation (3.7) is the optimum control that will produce minimum induced power.

$$C_P = \frac{1}{V} \{\theta\}^T [X_{sym}] \{\theta\} \tag{4.1.8}$$

Substitution of the optimum control into Eq. (3.8) yields

$$C_P = \left(\frac{1}{V} \right) \{C\}^T [Q_X]^{-1} \{C\} \tag{4.1.9}$$

where

$$[Q_X] = [D][P][X_{sym}]^{-1} [P]^T [D]^T \tag{4.1.10}$$

4.2 Finite Number of Blades without Inflow Coupling

Without inflow coupling, Eq. (3.3.7) can be expanded into a summation,

$$[P] = \sum_{k=-nQ}^{+nQ} [P]_k \quad (4.2.1)$$

where $[P]_k$ is defined as

$$\sum_{k=-nQ}^{+nQ} [P]_k = \sum_{k=-nQ}^{+nQ} \frac{\sigma a}{4} \cdot \left[[I] + \frac{\sigma a}{8V} [B]_0 [R]_k \right]^{-1} [A]_k \quad (4.2.2)$$

The optimization follows a procedure similar to that shown in section 4.2. It starts from the same definition of a functional, $F(\tau)$.

$$F(\tau) = C_P - \{C\}^T \{\Lambda\} \quad (4.2.3)$$

Substitution power, Eq. (3.2.3), and rotor loads into Eq. (4.2.3) yields:

$$\begin{aligned} F(\tau) &= \frac{1}{V} \sum_{k=-nQ}^{+nQ} \{\tau\}_{-k}^T [U] [R]_k \{\tau\}_k - \{\tau\}_0^T \{D\}^T \{\Lambda\} \\ &= \frac{1}{V} \{\theta\}^T \sum_{k=-nQ}^{+nQ} \left[[P]_{-k}^T [U]^T [R]_k [P]_k \right] \{\theta\} - \{\theta\}^T [P]_0^T \{D\}^T \{\Lambda\} \end{aligned} \quad (4.2.4)$$

For the simplicity, we define the following summation as $[Y]$.

$$[Y] = \sum_{k=-nQ}^{+nQ} \left[[P]_{-k}^T [U]^T [R]_k [P]_k \right] \quad (4.2.5)$$

With the exception of the fact that $[X]$ is replaced by $[Y]$, the remainder of the procedures are exactly the same as an infinite number of blades analysis. Therefore, only the final form of an optimum induced power is shown here.

$$C_P = \frac{1}{V} \{\theta\}^T [Y_{sym}] \{\theta\} \quad (4.2.6)$$

Substitution of the optimum control into Eq. (4.2.6) yields:

$$C_P = \left(\frac{1}{V} \right) \{C\}^T [Q_Y]^{-1} \{C\} \quad (4.2.7)$$

where

$$[Q_Y] = [D][P]_0 [Y_{sym}]^{-1} [P]_0^T [D]^T \quad (4.2.8)$$

4.3 Finite Number of Blades with Inflow Coupling

Since we include inflow coupling $[\bar{P}]$ is used throughout the optimization process in this chapter instead of $[P]_k$. Following the exact same procedure as in the previous section produces the optimum power equation.

$$\begin{aligned} F(\bar{\tau}) &= \frac{1}{V} \{\bar{\tau}\}^T [U][\bar{R}]\{\bar{\tau}\} - \{\tau\}_0^T \{D\}^T \{\Lambda\} \\ &= \frac{1}{V} \{\theta\}^T [\bar{P}]^T [U]^T [\bar{R}][\bar{P}] - \{\theta\}^T [P]_0^T \{D\}^T \{\Lambda\} \end{aligned} \quad (4.3.1)$$

To simplify the algebra, we define the following grouping as $[Z]$:

$$[Z] = [\bar{P}]^T [U]^T [\bar{R}][\bar{P}] \quad (4.3.2)$$

The final form of the optimum induced power is

$$C_P = \frac{1}{V} \{\theta\}^T [Z_{sym}] \{\theta\} \quad (4.3.3)$$

Substitution of the optimum control into Eq. (4.3.3) yields:

$$C_P = \left(\frac{1}{V} \right) \{C\}^T [Q_Z]^{-1} \{C\} \quad (4.3.4)$$

where

$$[Q_Z] = [D][P]_0 [Z_{sym}]^{-1} [P]_0^T [D]^T \quad (4.3.5)$$

Eq. (4.3.4) is a closed form, compact induced power equation which is the final goal of this dissertation. Entire theory developed in this dissertation was to obtain Eqs. (4.1.9), (4.2.7), and (4.3.4).

4.4 Normalization of the Power Equation

Since induced power is the power associated with the lift produced by the rotor, it is appropriate to normalize the induced power by the rotor thrust. Dividing both sides of Eq. (4.1.9) by C_T^2 yields:

$$\frac{C_P}{C_T^2} = \left(1/V\right) \left(\{C\}^T / C_T \right) [Q_{XorYorZ}]^{-1} \left(\{C\} / C_T \right) \quad (4.4.1)$$

$$\left(\frac{C_P}{C_T^2} \right)_{\text{optimum}} = \left(1/V\right) \{\bar{C}\}^T [Q_{XorYorZ}]^{-1} \{\bar{C}\} \quad (4.4.2)$$

Eq. (4.4.2) can be compared to the Glauert ideal induced power for a lifting rotor at a high advance ratio, which is given by

$$\left(\frac{C_P}{C_T^2} \right)_{\text{ideal}} = \frac{1}{2\mu} \quad \leftrightarrow \quad \left(\frac{C_P}{C_T^2} \right)_{\text{optimum}} = \left(1/V\right) \{\bar{C}\}^T [Q_{XorYorZ}]^{-1} \{\bar{C}\} \quad (4.4.3)$$

The calculated induced power should never be lower than the Glauert minimum.

4.5 Solution Convergence Methods

It is important to know how results converge as the dynamic model is expanded to include more harmonics and more radial functions. Two methods seen in Fig. 4.1, are used to study this. The first is the table method, and the second is the rectangular method. The differences between these two methods are explained in Appendix A. For an infinite number of blades, solutions converge faster by using the rectangular method than using the table method, and this work uses the rectangular method accordingly.

For a finite number of blades, though, results using table method are shown because result obtained by table method converge faster than those obtained from the rectangular method.



Figure 4.1. Rectangular and table convergence methods

5. Results with an Infinite Number of Blades

The use of conventional collective and cyclic pitch control with no twist and an infinite number of blades is treated in the first part of this chapter. Later, higher harmonic control and twist are added. Both collective and cyclic pitch are used in tandem to achieve a specified thrust and to trim the rotor to zero resultant pitch and roll moment. A propulsive force trim constraint is not applied.

The title of each figure includes values for M, N, H, and D. In that context, M is the maximum harmonic number, and N is the number of polynomials used. Both M and N are related to the convergence of the solution. Higher values of M and N produce a more converged solution. H is the maximum harmonic of the blade pitch control, and D is the maximum order of the blade radial twist.

Induced Power Results with Classical Control

In this section, $H = 1$ and $D = 0$ are used for every figure. $H=1$ implies no higher harmonic control, and $D=0$ implies that the blade is untwisted. A solution with $M=H+2$ and $N=100$ can be considered as “fully converged” which means a total number of 700 states are used to achieve full convergence.

Without Reverse Flow

To begin the analysis, we repeat the results of Refs. [14] and [15] (with no reverse flow) but with more states in the dynamic wake model than were used by File. Due to computer limitations and the presence of ill-conditioned matrices, File was able to use only 45 states in his analysis. Here, by using more efficient algorithms and by using the rectangular method, we have been able to obtain a fully converged solution.

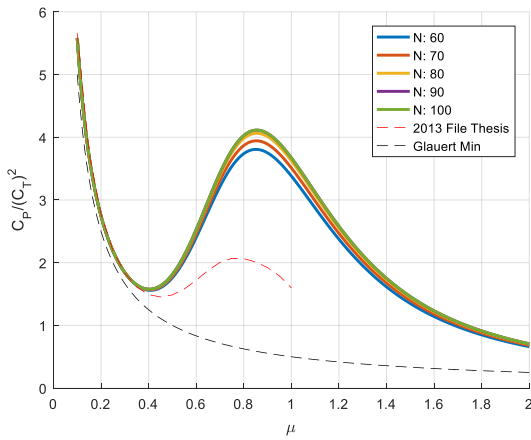


Figure 5.1. Fully converged induced power without reverse flow, $M=3$.

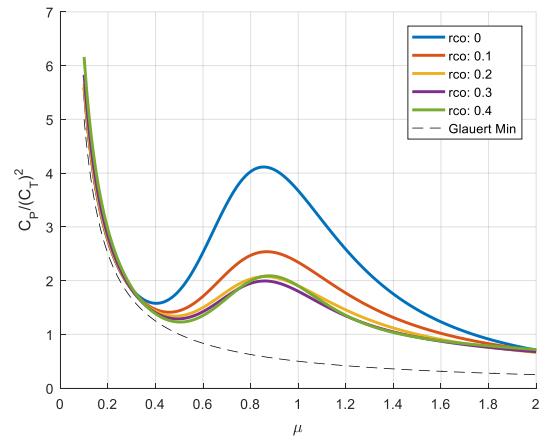


Figure 5.2. Effect of root cut-out without reverse flow, $M=3$, $N=100$.

Figure 5.1 shows the results of File and the present, fully converged results. Even fully converged solutions do not show a singularity in induced power with no reverse flow. In other words, the power requirement does not go to infinity at the critical advance ratio.

Next, we compute induced power with various root cut-out (rco) values. Figure 5.2 shows that, as rco increases from zero to 0.3, the overall power consumption decreases. The reason behind this continuous reduction in power is related to how inflow and pressure are distributed throughout the rotor disk.

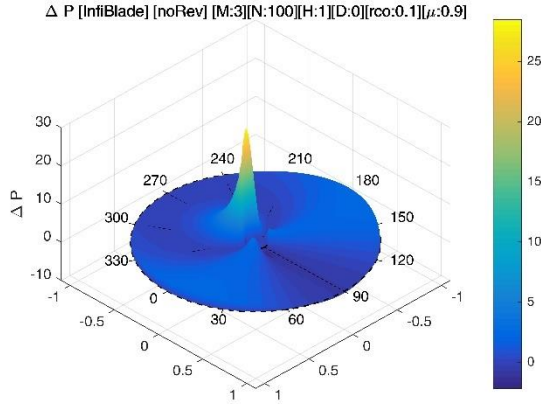


Figure 5.3. Non-dimensional pressure distribution across the disk with $rco=0.1$, $\mu=0.9$, $N=100$.

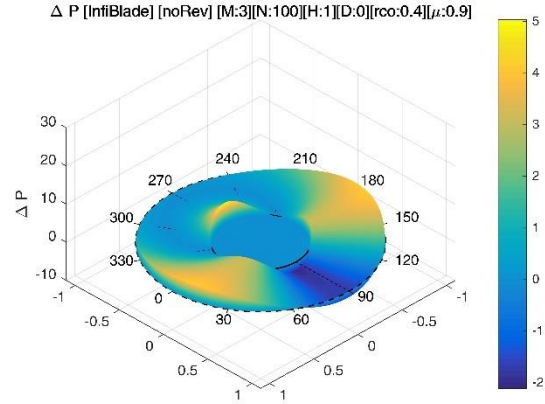


Figure 5.4. Pressure distribution across the disk with $rco=0.4$, $\mu=0.9$, $N=100$.

The pressure peak near the root region is shown in Fig. 5.3. The condition of small root cut-out and no reverse flow causes the pressure to be concentrated in a small region. High power consumption is caused by this small region of high pressure because power is the product of inflow and pressure distribution.

The introduction of moderate root cut-out removes this small region of high pressure, causing the loads and inflow distribution to be spread out more evenly throughout the disk. Figure 5.4 shows how the introduction of root cut-out = 0.4 spreads out the pressure distribution over a larger area, as compared to that of Fig. 5.3.

Effect of Reverse Flow

Figure 5.5 shows the induced power behavior when reverse flow is added to the model.

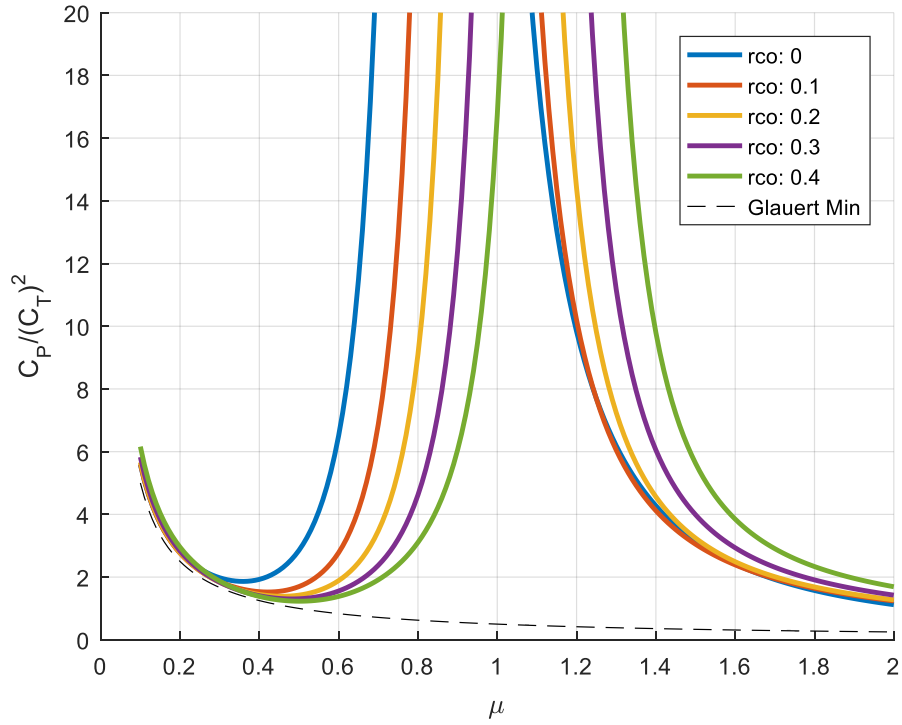


Figure 5.5. Effect of root-cutout with reverse flow, no inflow feedback, $M=3$, $N=100$.

The induced power becomes infinite near the critical advance ratio in the presence of reverse flow. This plot shows that a direct analytical method can indeed reproduce the singular behavior of the rotor power as predicted by Ormiston (and also confirmed by Hall and Giovanetti).

As advance ratio increases, cyclic pitch is imposed to satisfy the zero hub moment trim condition.

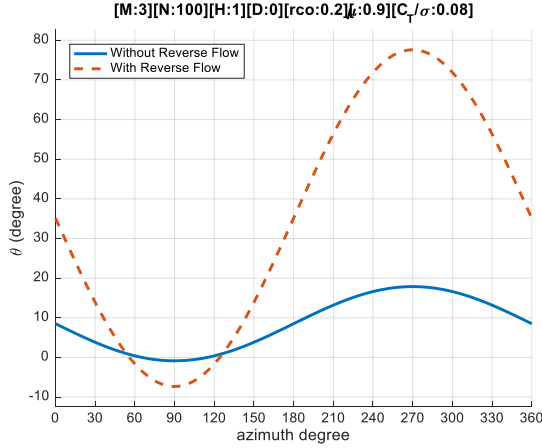


Figure 5.6. Pitch angle with and without reverse flow.

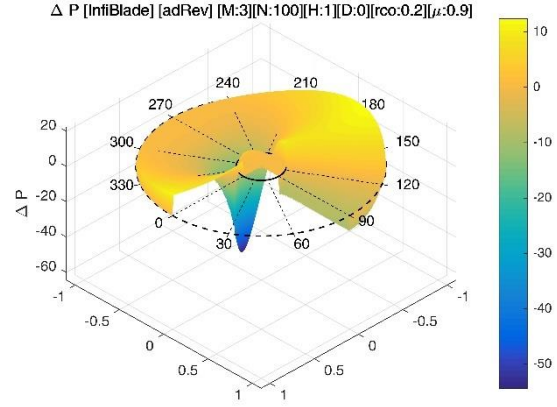


Figure 5.7. Non-dimensional pressure distribution across the rotor with reverse flow.

Figure 5.6 shows the blade pitch angle both with and without reverse flow. When reverse flow is added to the analysis, the pitch on the advancing blade decreases, while the pitch on the retreating blade increases. These changes occur more rapidly when reverse flow is included than when reverse flow is not included. As a result of the trim constraint, the inboard portion of the blade in the reverse flow region produces negative lift, while the remainder of the rotor produces positive lift, as shown in Fig. 5.7. This highly non-uniform rotor lift distribution causes induced power to increase. In fact, at the critical advance ratio, induced power is increased to infinity because we let the pitch increase up to infinity. If we instead use finite pitch, the resulting induced power will also be finite, shown in Fig. 5.5. However, letting pitch to go to infinity is necessary because otherwise negative lift in the reverse flow region completely cancels the positive lift, making the net lift equal to zero: The rotor cannot maintain its required thrust.

Figure 5.5 also shows that changing the value of root cut-out shifts the critical advance ratio and the point of singularity. This makes physical sense in that, as root cut-out is increased, the region of reverse flow is diminished; and thus the critical advance ratio shifts to higher values with increasing root cut-out.

Effect of Inflow Feedback and Reverse Flow

The effect of inflow feedback is added to that of reverse flow in Fig. 5.8. The magnitude of inflow feedback is controlled by changes in σ , the solidity. (Solidity is the percentage of the rotor disk covered by blade area.)

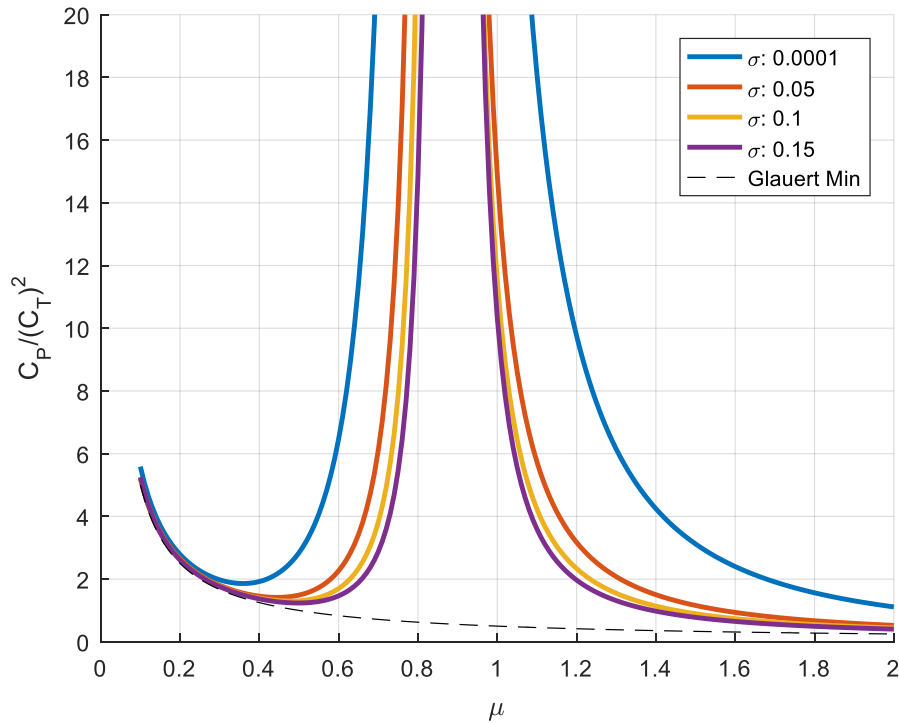


Figure 5.8. Effect of inflow feedback with reverse flow, no root cutout, $M=3$, $N=100$.

The overall induced power decreases with increased inflow feedback (i.e., with increased solidity). The singular peak narrows when solidity is increased. Inflow feedback forces the lift distribution into a more nearly ideal shape so that the induced power decreases.

Induced Power Results with Higher Harmonic Control

This section focuses on the effect of higher harmonic control ($H \geq 1$ and $D \geq 0$). Other than that, analysis in this section uses same conditions as for the results for conventional control shown earlier.

Without Reverse Flow

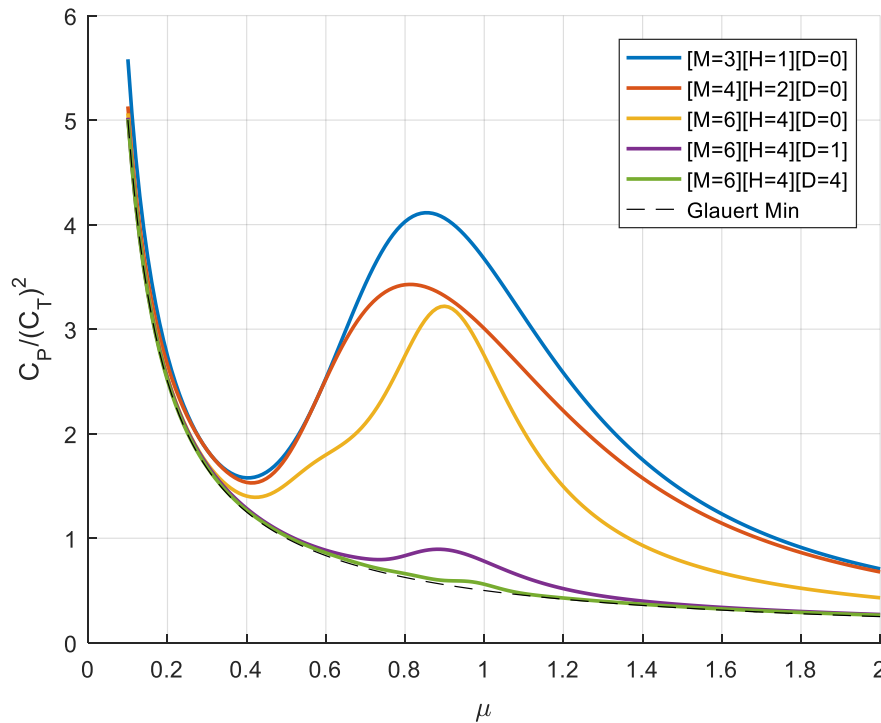


Figure 5.9. Effect of HHC control without reverse flow, no root cutout, $N=100$.

In Refs. [14] and [15], File showed that power decreases with HHC control. However, as seen from Fig. 5.1, his results were not fully converged. Fully converged HHC solutions are presented in Fig. 5.9. As the number of control degrees of freedom is increased, induced power decreases and eventually approaches the Glauert minimum.

Effect of Reverse Flow and Inflow Feedback

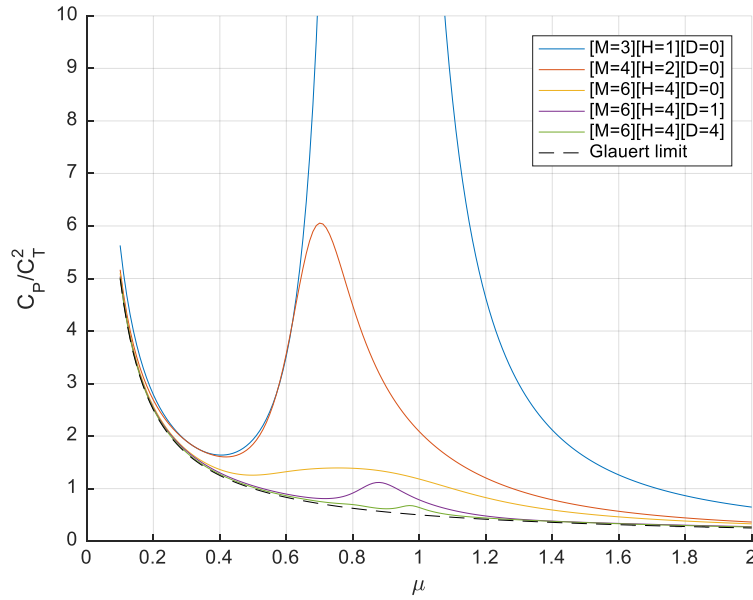


Figure 5.10. Effect of HHC control with reverse flow, no root cutout, $N=10$.

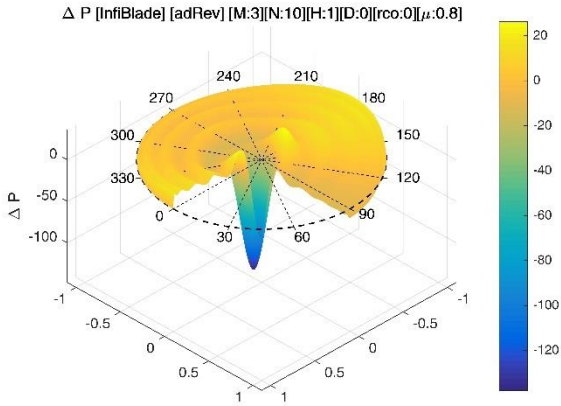


Figure 5.11. Non-dimensional pressure distribution across the disk with reverse flow, $H=1$, $N=10$, $\mu=0.8$.

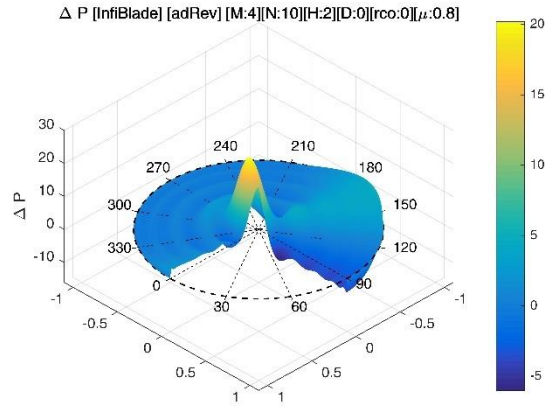


Figure 5.12. Non-dimensional pressure distribution across the disk with reverse flow, $H=2$, $N=10$, $\mu=0.8$.

Figure 5.10 shows that HHC control removes the infinite power peak. Increasing H from 1 to 2 is enough to remove the singularity. This removal of the infinite power peak can be explained with the use of the non-dimensional pressure plots in Figs. 5.11 and 5.12. The negative pressure peak in Fig. 5.11 is turned into a positive peak in Fig. 5.12 when H is increased from 1 to 2. Figure

5.10 shows that even with the presence of the reverse flow, use of $H=4$ and $D=4$ reduces the power to nearly the Glauert minimum.

Effect of Inflow Feedback and Reverse Flow

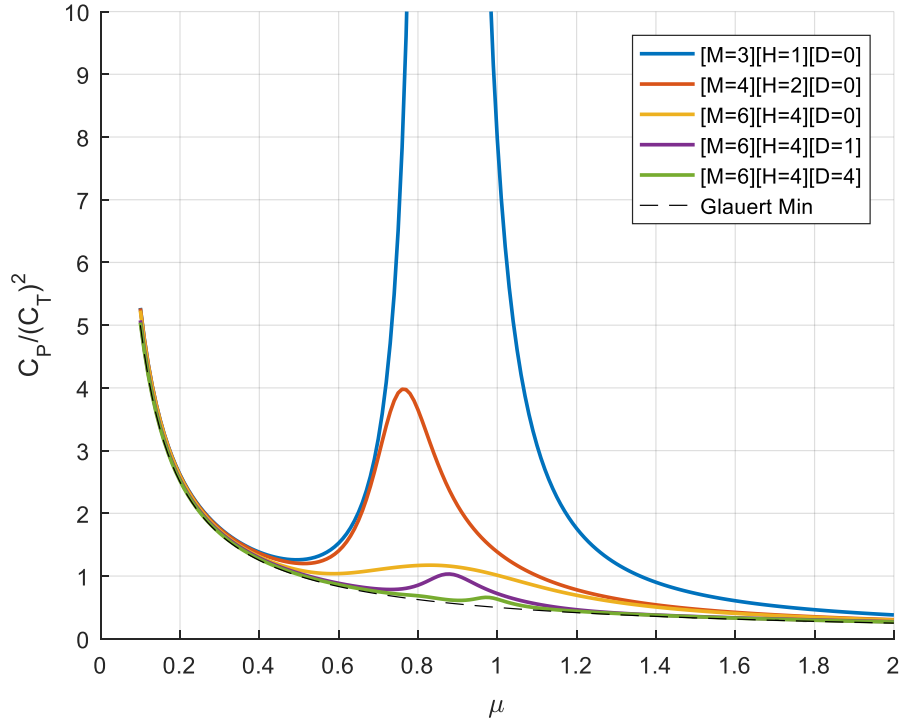


Figure 5.13. Effect of HHC control with reverse flow and inflow feedback, no root cutout, solidity=0.15, $N=10$.

Inflow feedback causes the power peaks in Fig. 5.13 to be lower and narrower than those in Fig. 5.10. Therefore, we can conclude that, in these cases, inflow feedback reduces the induced power requirement. No matter how many controls are used, the inclusion of inflow feedback does not appear to increase the power consumption.

Magnitude of Optimum Blade Pitch with Realistic Thrust

Plots in this section show blade pitch around the azimuth in degrees for three different advance ratios: 0.4, 0.8, and 1.2. A realistic C_T /solidity of 0.08 is chosen to show realistic pitch behavior with and without reverse flow.

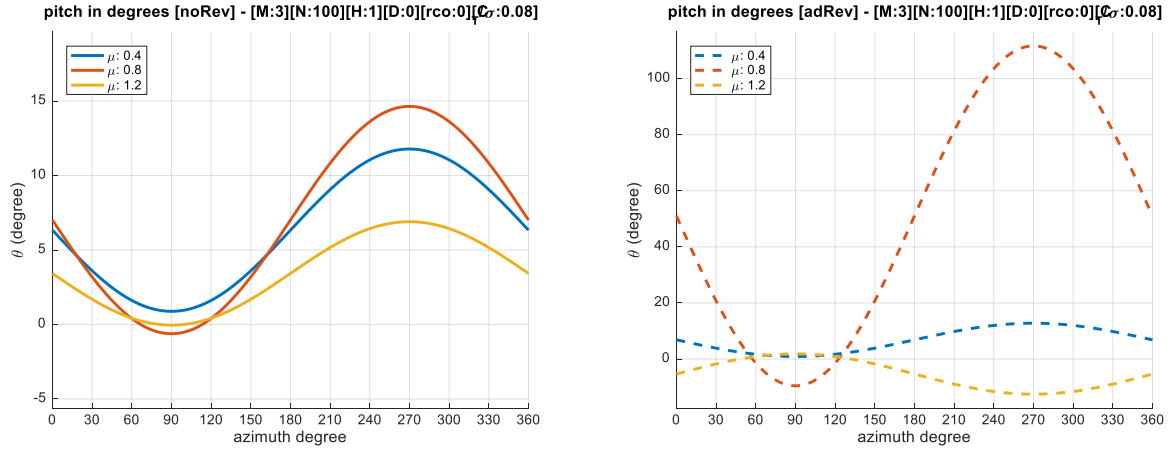


Figure 5.14. Realistic blade pitch without (left) and with (right) reverse flow using conventional collective cyclic pitch control to trim, and three advance ratios.

Fig. 5.14 shows that when $\mu = 0.4$ (blue curves), the pitch angle behaves similarly with and without reverse flow. The assumption of no stall on the airfoil is valid at this advance ratio because the lowest and highest peaks are around 2° and 13°, respectively. However, for $\mu = 0.8$ and 1.2, results with and without reverse flow show large differences in pitch behavior. The maximum pitch angle for $\mu = 0.8$ without reverse flow is around 15°, while that value with reverse flow is over 100°, which is not practical. This is the point at which the assumption of no stall fails, because the blade would experience stall at this unrealistically high pitch angle. For $\mu = 1.2$, in the case of no reverse flow, the pitch angle has both negative peak on the advancing side and positive peak on the retreating side. However, with reverse flow, the pitch angle has peaks of opposite sign as compared to no reverse flow.

Non-Dimensional Pressure and Inflow Distributions

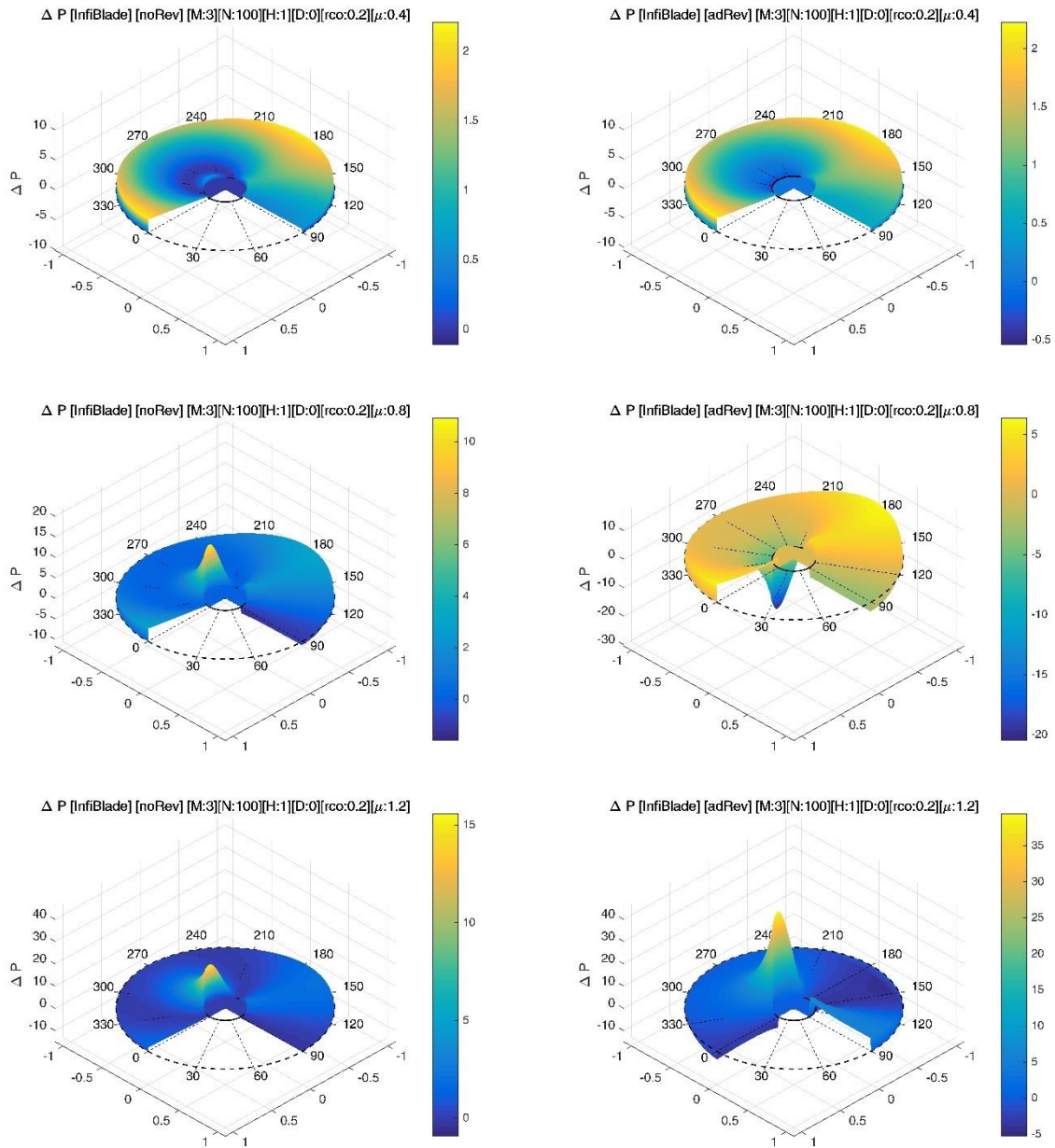
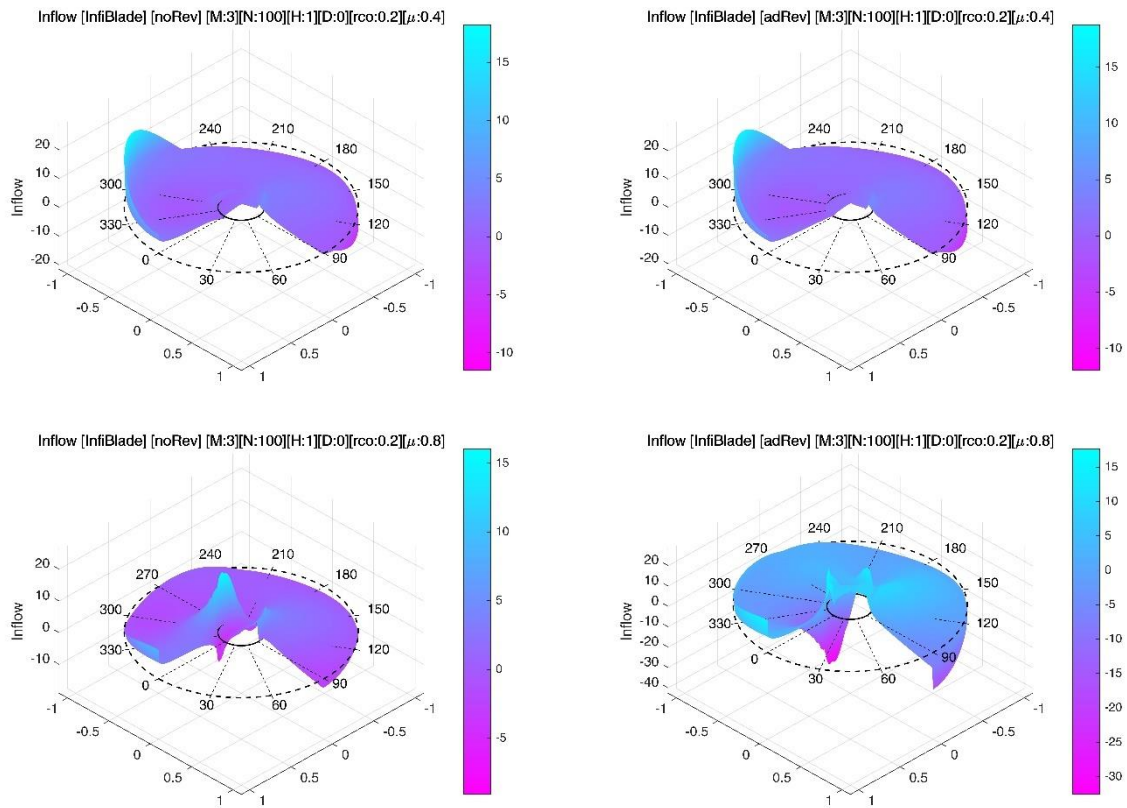


Figure 5.15. Non-dimensional pressure distributions with and without reverse flow, for three advance ratios.

The plots in Fig. 5.15 can be considered as a 3x2 table. The left and right columns represent cases without and with the reverse flow, respectively. Each row represents a different value of advance ratio: $\mu = 0.4, 0.8, \text{ and } 1.2$ from the top to bottom row. For the lowest advance ratio,

pressure distributions show similar patterns either with or without reverse flow: There are no pressure peaks. For $\mu = 0.8$, peaks having opposite signs are found on the retreating side of the rotor with or without reverse flow. For $\mu = 1.2$, positive peaks occur on the retreating side of the rotor both with and without reverse flow. The amplitude of the peaks is higher with reverse flow than it is with no reverse flow. The higher amplitudes seen for $\mu = 1.2$ cause larger induced power with reverse flow than without. The figure below gives the corresponding inflow distribution for the pressure distributions shown in Fig. 5.15.



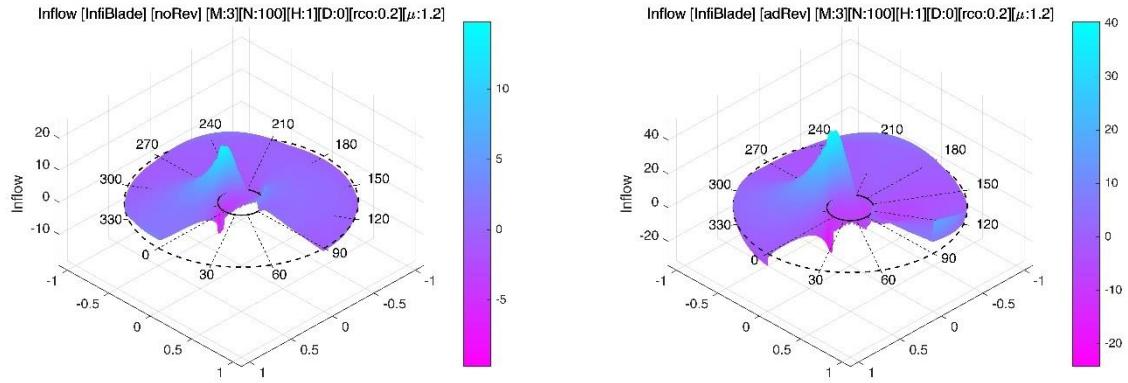


Figure 5.16. Non-dimensional inflow distribution with and without reverse flow, for three advance ratios.

6. Results with a Finite Number of Blades

This chapter presents results for a finite number of blades. The title of each figure in this section includes the values of Q (blade number), M (maximum harmonic number), H (maximum harmonic of blade control), and D (maximum polynomial order of blade twist) that are used in the figure. The number of blades, Q , is varied from 2 to 12. For every maximum harmonic M , the table method of Ref. [12] is used, which implies a maximum polynomial index (N) for the finite-state model of $N = M+1$. As M and N thus increase together, the solution converges. To simulate the “rubber rotor” of Ref. [4], H and D can be considered as infinity, since the pitch angle is unconstrained as a function of time and radius.

Comparisons of Results with Hall and Hall⁴, Hall and Giovanetti¹⁶, and Ormiston⁹

Due to the seemingly insurmountable obstacle of the algebra of closed-form solutions with a finite number of blades, previous induced power results by the finite-state method were obtained only for an infinite number of blades, Refs. [10-11], [15], and [18-20]. On the other hand, the numerical results available for comparisons were obtained for a finite number of blades, Refs. [4], [9], and [16]. In all of three works, direct comparison between analytical and numerical results was not possible. However, this dissertation has overcome the algebraic obstacles (see Chapter 3), so that now numerical and analytical results can be directly compared. Induced power results from

Hall and Hall⁴, Hall and Giovanetti¹⁶, and Ormiston⁹ are therefore compared with finite-state methods in the results to follow.

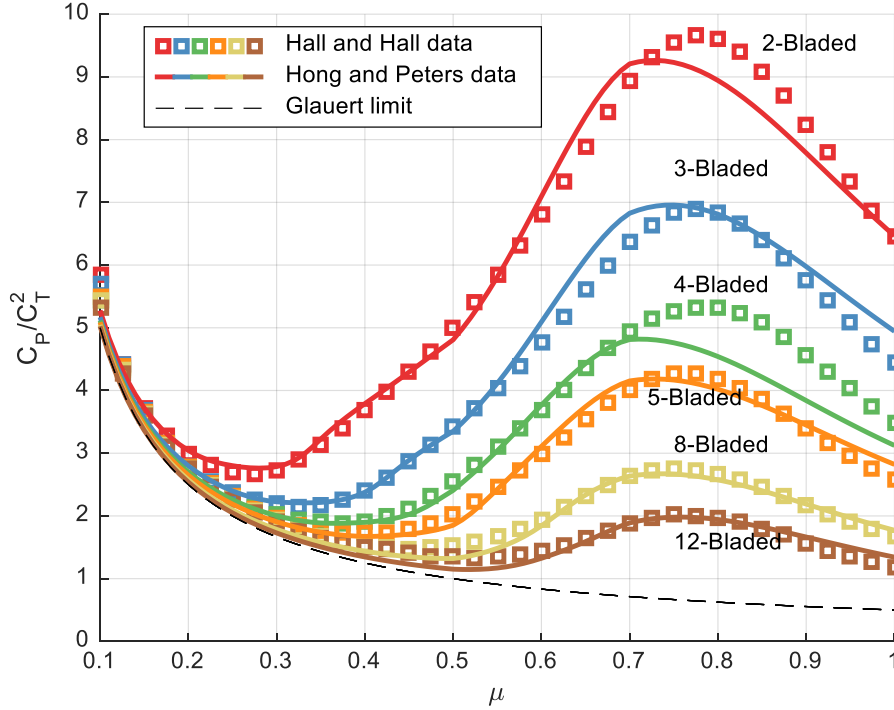


Figure 6.1. Rubber blade minimum induced power comparison between present and Hall and Hall⁴, $M:60$, $rc:0.1$.

Figure 6.1 shows normalized induced power as a function of advance ratio for an optimized blade at varying blade numbers. For the Hall and Hall results, Ref. [4], the blade is assumed to have no stall and to be able to have any angle of attack as a function of radius and time. For our results, we varied the non-dimensional chord, \bar{b} , to match the Hall and Hall results from Ref. [4]. The blade semi-chord has only a minor effect on the final answer, but it does affect the convergence. Thus, we chose the \bar{b} with the best convergence. Both results show similar optimum induced power behavior—as the number of blades decreases, induced power increases. Reference [4] notes that the increase in induced power near $\mu=0.8$ is due to gaps in the shed wake. As the number of

blade decreases, the size of these gaps increases, which causes the induced power to increase. While Ref. [4] used the velocity in the far wake for their induced power computation, this dissertation uses a near-wake analysis. As a consequence, the reason behind the induced power dependency on the blade number is seen from a different perspective here.

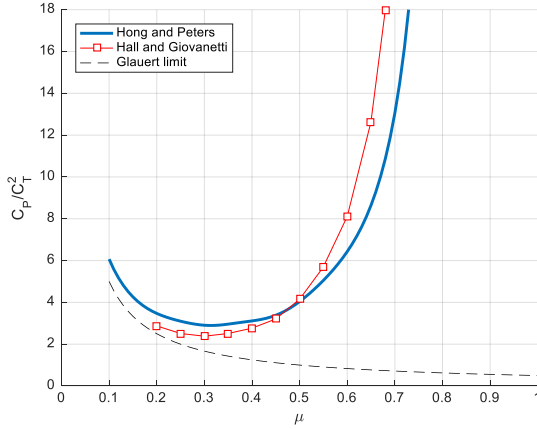


Figure 6.2. Comparison of induced power results with Hall and Giovanetti¹⁶, $Q:4$, $M:12$, $rco:0.1$, $\sigma:0.1157$.

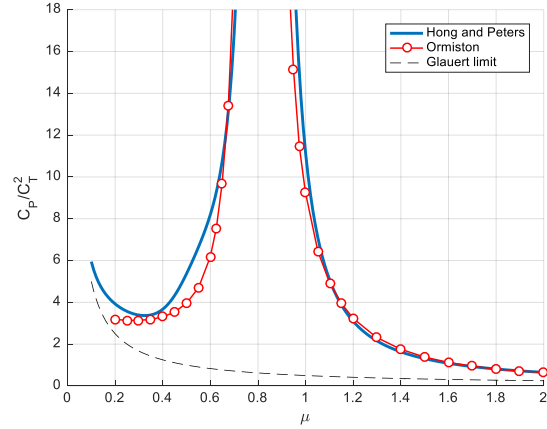


Figure 6.3. Comparison of induced power results with Ormiston⁹, $Q:3$, $M:12$, $rco:0$, $\sigma:0.111$.

Figures 6.2 and 6.3 show the induced power for a 4-bladed rotor without stall that uses only conventional collective and cyclic pitch to trim. The results of Hall and Giovanetti¹⁶ are represented by the red squares in Fig. 6.2. They used a vortex lattice model to obtain their results. The two results in Fig. 6.2 show similar behaviors. Minor differences might be because the two methods use different representations of blade twist. While the present analysis uses no twist, results from Hall and Giovanetti use a fixed twist optimized at each advance ratio. The results of Ormiston⁹ are indicated by the red curve in Fig. 6.3. These results were obtained by application of the U.S. Army code "Rotorcraft Comprehensive Analysis System" (RCAS). The results shown in Fig. 6.3 show good agreement with each other, which verifies the approach of this thesis to finding closed-form induced power from the finite-state inflow theorem.

Results with Classical Control

This section treats rotors with only classical collective and cyclic pitch, which implies $H = 1$ and $D = 0$ are used for all results. $H = 1$ implies no higher harmonic control, and $D = 0$ implies the blade is untwisted. Three different aerodynamic assumptions are analyzed in this section: 1) no reverse flow, 2) with reverse flow, and 3) with inflow feedback and reverse flow.

Without Reverse Flow

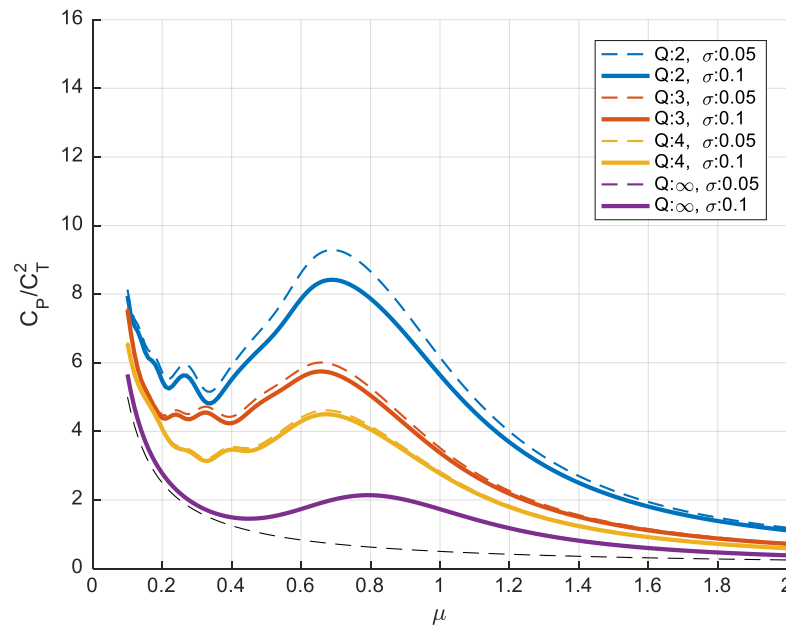


Figure 6.4. Induced power without reverse flow for varied blade numbers and solidity values, $M:12$, $rco:0$

Figure 6.4 shows induced power for variations in blade numbers and solidity with no reverse flow. Rotors are considered with blade numbers varying from 2 to infinity, and each blade number is analyzed for two different values of solidity, 0.05 and 0.1. When reverse flow is not included,

induced power displays a finite peak. Figure 6.4 shows that the induced power of the rotor decreases as the number of blades increases. This is consistent with the findings of Hall and Hall in Ref. [4]. They state that the reason behind this inversely proportional relationship is the gaps in the wake that develops on the retreating side of the disk. As the number of blades increases, the size of the gaps in the wake decreases, which causes the induced power to decrease.

The results with an infinite number of blades show no differences in induced power with varied solidity values. However, for a finite number of blades, induced power is slightly higher when lower solidity is used. Induced power is dependent on solidity because the finite-state inflow model spreads out the pressure loading on the disk over a finite chord length. A higher solidity with the same number of blades means a wider chord. When the chord is wider, pressures are distributed over a wider area, as shown in Figs. 6.5 and 6.6.

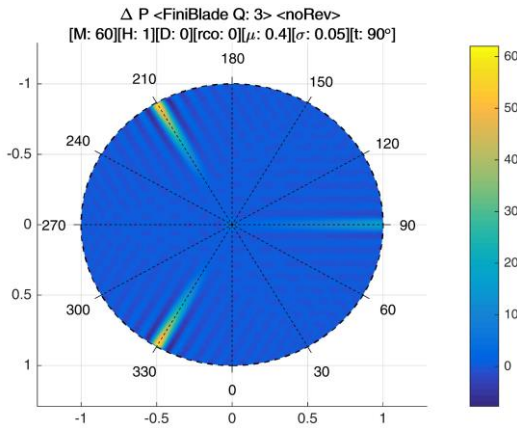


Figure 6.5. Pressure distribution with narrower solidity.

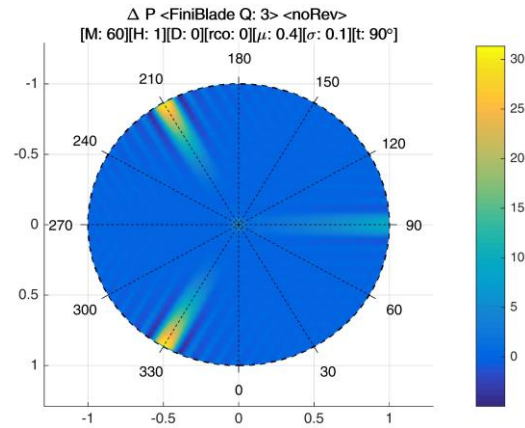


Figure 6.6. Pressure distribution with wider solidity.

Figures 6.5 and 6.6 show snapshots of the pressure distribution on the rotor. The figures reveal that, for the same lift, the pressure distribution with the larger solidity has smaller pressure peaks than does the pressure for the rotor with lower solidity. Since induced power is the product of pressure and inflow, lower pressure peaks cause lower induced power, as was seen in Fig. 6.4.

Effect of Reverse Flow and Inflow Feedback

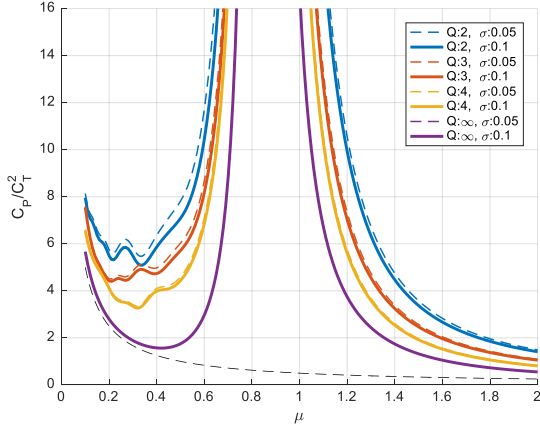


Figure 6.7. Induced power with reverse flow effect for varied blade numbers and solidity, $M:12$, $rco:0$

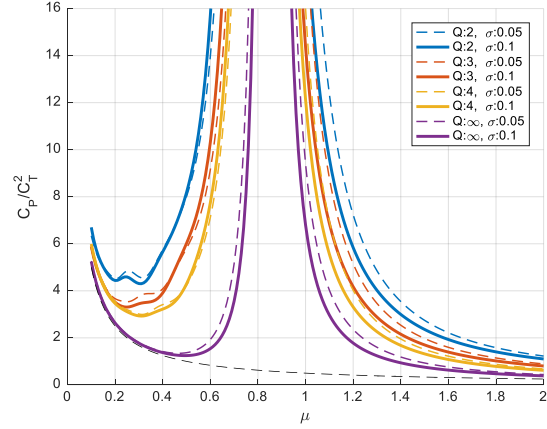


Figure 6.8. Induced power with reverse flow and inflow feedback effects for varied blade numbers and solidity, $M:12$, $rco:0$.

Figure 6.7 shows induced power for varied in blade numbers and solidity with reverse flow. The induced power increases to infinity at a critical advance ratio when the reverse flow is added. Many previous studies (Refs. [9], [16], [18]) have shown this same singularity in induced power at high advance ratios. Once again, higher solidity produces lower induced power for a finite number of blades. The induced power for a rotor with an infinite number of blades does not change with variations of solidity when the effect of inflow feedback is not included.

Figure 6.8 shows induced power for varied blade numbers and solidity, with both reverse flow and inflow feedback. In Fig. 6.8, higher solidity implies a larger effect of inflow feedback. Higher solidity produces lower induced power for a rotor with an infinite number of blades. However, for a finite number of blades, higher solidity does not necessarily produce lower induced power. Inflow feedback can either lower or raise induced power, because the angle of attack from inflow can move the loading distribution either closer to or further away from the optimum.

Comparison between Finite and Infinite Numbers of Blades

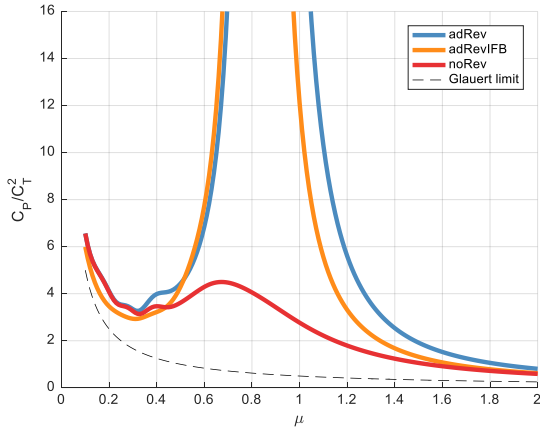


Figure 6.9. Effects of assumptions on induced power, $Q:4$, $M:12$, $rco:0$, $\sigma: 0.1$.

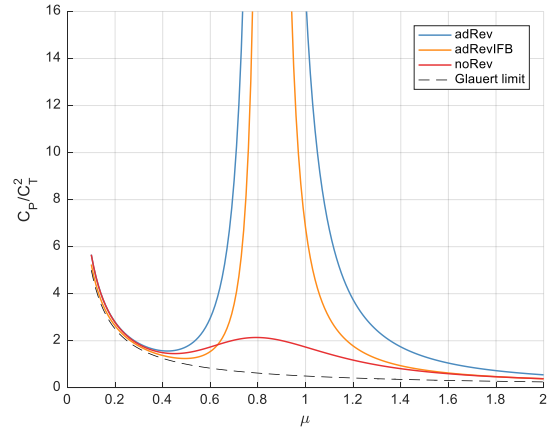


Figure 6.10. Effects of assumptions on induced power, $Q:\infty$, $M:12$, $rco:0$, $\sigma: 0.1$.

Figures 6.9 and 6.10 show how the assumptions of no reverse flow, with reverse flow, or with reverse flow and inflow feedback alter the induced power for a rotor with either a finite or an infinite number of blades. The main difference can be seen in the advance ratio range of 0.5 to 0.8: For the infinite number of blades in Fig. 6.10, the addition of inflow feedback reduces the induced power, while the opposite is true in Fig. 6.9 for a finite number of blades.

Results with Higher Harmonic Controls

This section focuses on the effect of higher harmonic controls. ($H \geq 1$ and $D \geq 0$).

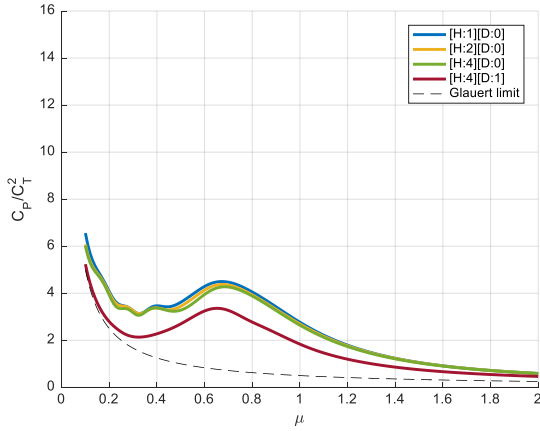


Figure 6.11. The effect of HHC on induced power without reverse flow and inflow feedback, $Q:4$, $M:12$, $rco:0$, $\sigma:0.1$.

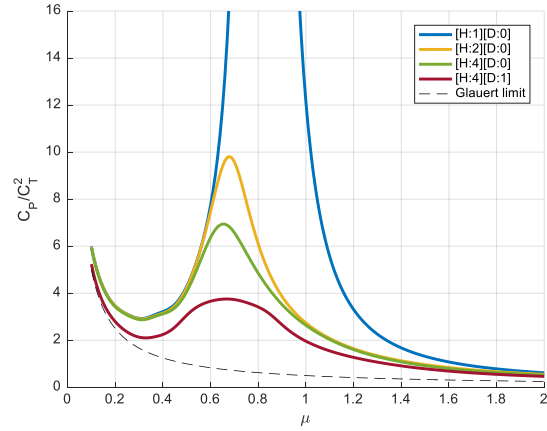


Figure 6.12. The effect of HHC on induced power with reverse flow and inflow feedback, $Q:4$, $M:12$, $rco:0$, $\sigma:0.1$.

The addition of a conventional higher harmonic control input (i.e, H increased from 1 to 4) does not reduce power by an appreciable amount when there is no reverse flow or inflow feedback, Fig 6.11. However, when linear radial twist is included (D is increased from 0 to 1), induced power shows a noticeable decrease. On the other hand, in Fig. 6.12, in which reverse flow and inflow feedback are included, an increase in H from 1 to 2 (i.e., the addition of two-per-rev higher harmonic control) is enough to remove the singularity in power that occurs near $\mu = 0.8$. This same effect was shown in Ref. [18], which considered an infinite number of blades. Therefore, for realistic aerodynamic assumptions, the added degrees of freedom of HHC control always reduce the induced power, and the reduction is dramatic at a high advance ratio.

Non-Dimensional Pressure and Inflow Distributions

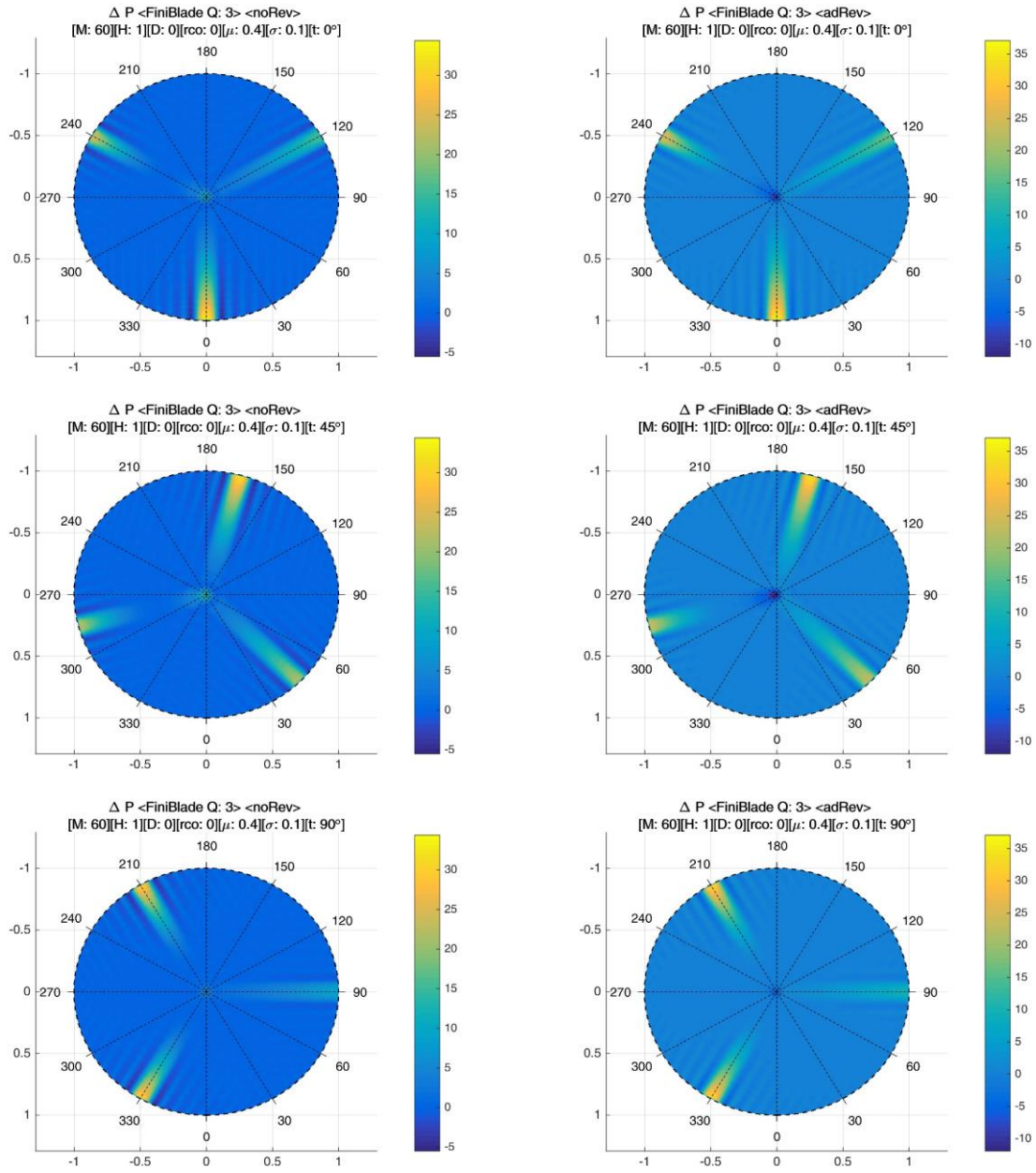


Figure 6.13. Pressure distributions both without and with reverse flow, $\mu=0.4$.

The plots in Fig. 6.13 form a 2x3 table. The left column represents cases without reverse flow and right column represents cases with reverse flow. Each row represents a different value of

dimensionless time in degrees: 0° , 45° and 90° , from left to right. All the plots are for an advance ratio $\mu = 0.4$ and pressure distributions either with or without reverse flow show similar patterns.

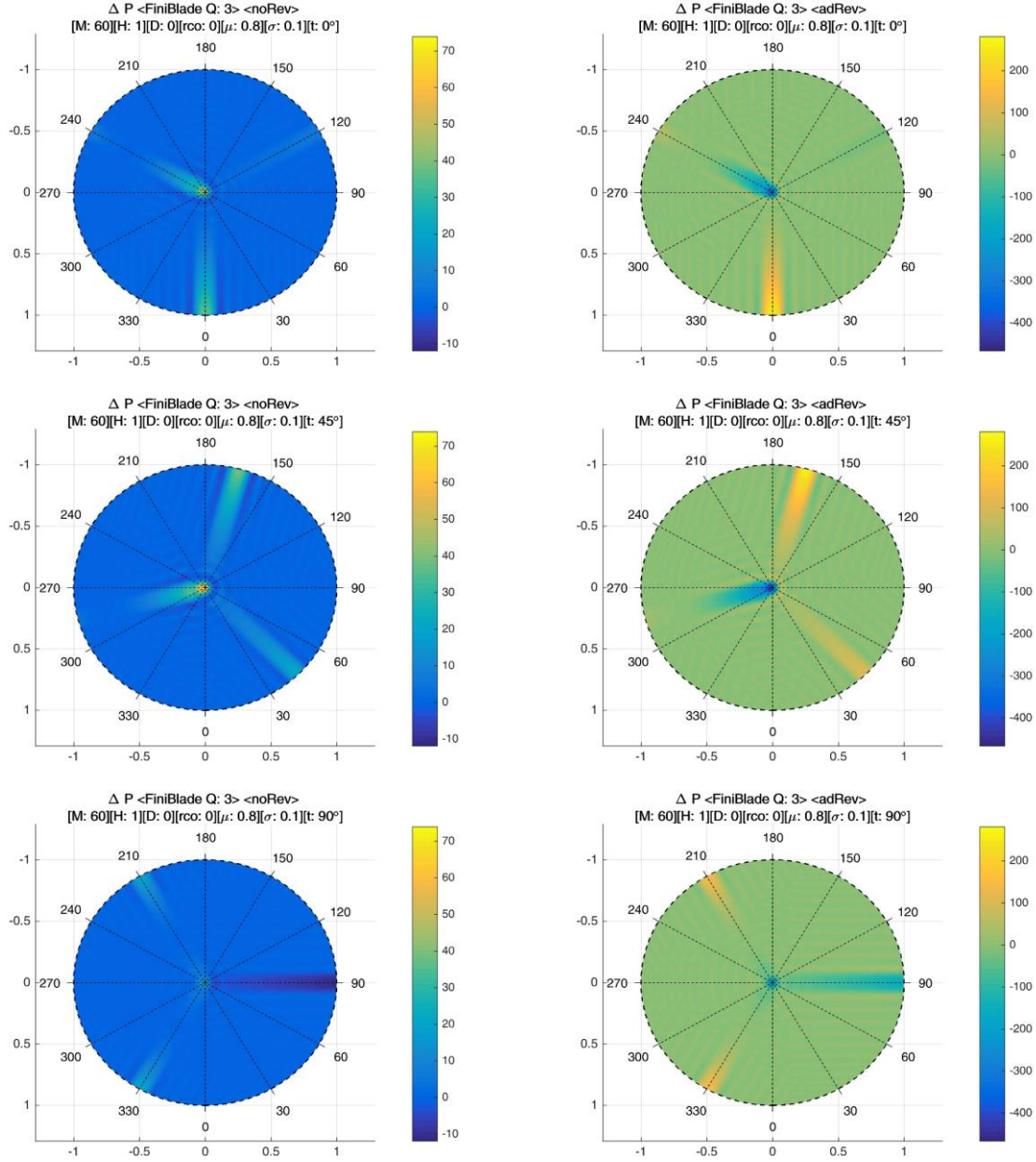


Figure 6.14. Pressure distributions both without and with reverse flow, $\mu = 0.8$.

Figure 6.14 is the same as 6.13, except that advance ratio is changed from $\mu = 0.4$ to 0.8 . At this critical advance ratio, the pressure distributions (either with or without reverse flow) exhibit large differences. The biggest difference is that at $\mu = 0.8$ the pressure peaks near the root of the

retreating side have a sign that is opposite to their sign without reverse flow. The figures below give the corresponding inflow distributions for pressure distribution shown in Figs. 6.13 and 6.14.

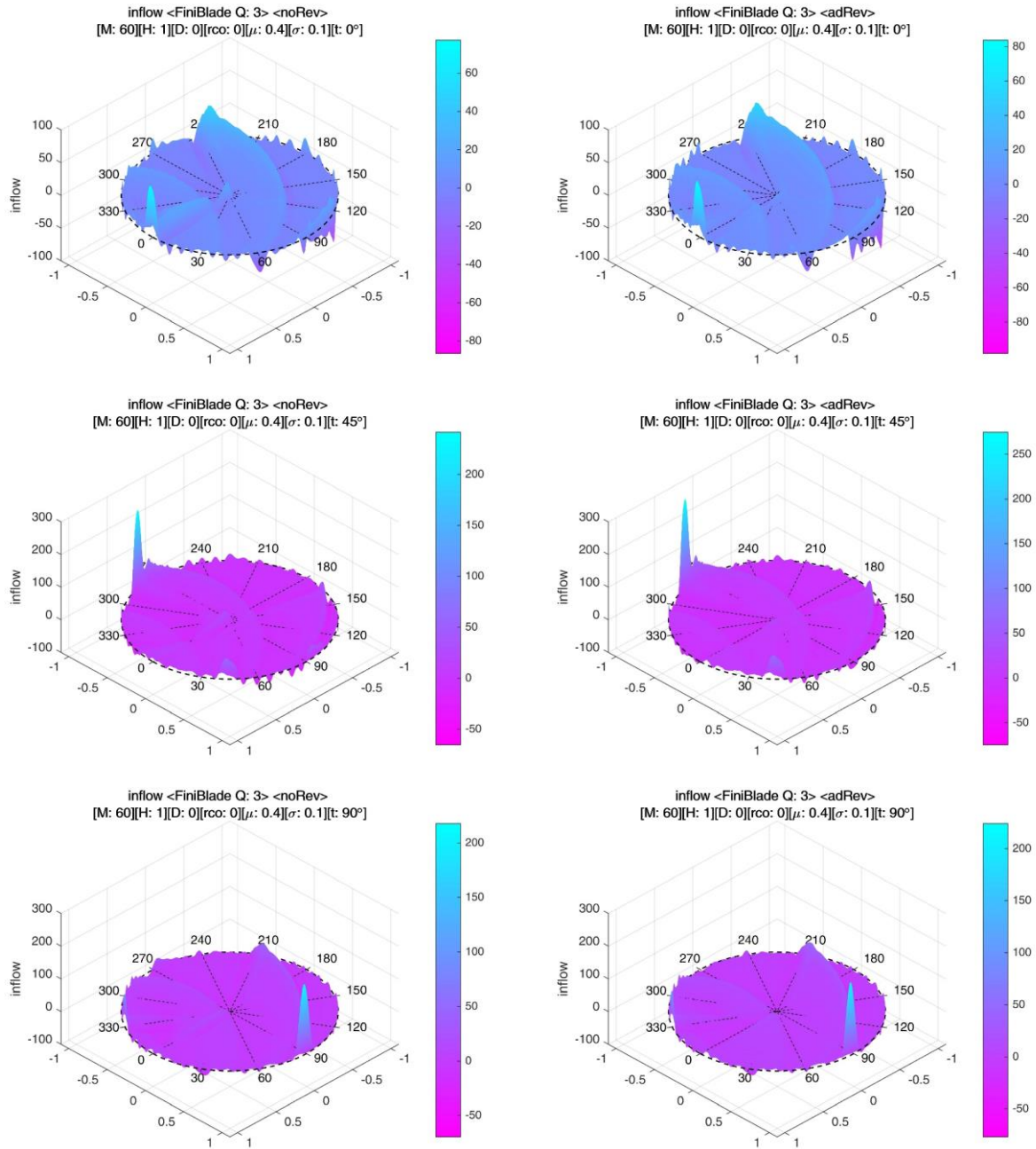


Figure 6.15. Inflow distribution both without and with reverse flow, $\mu=0.4$.

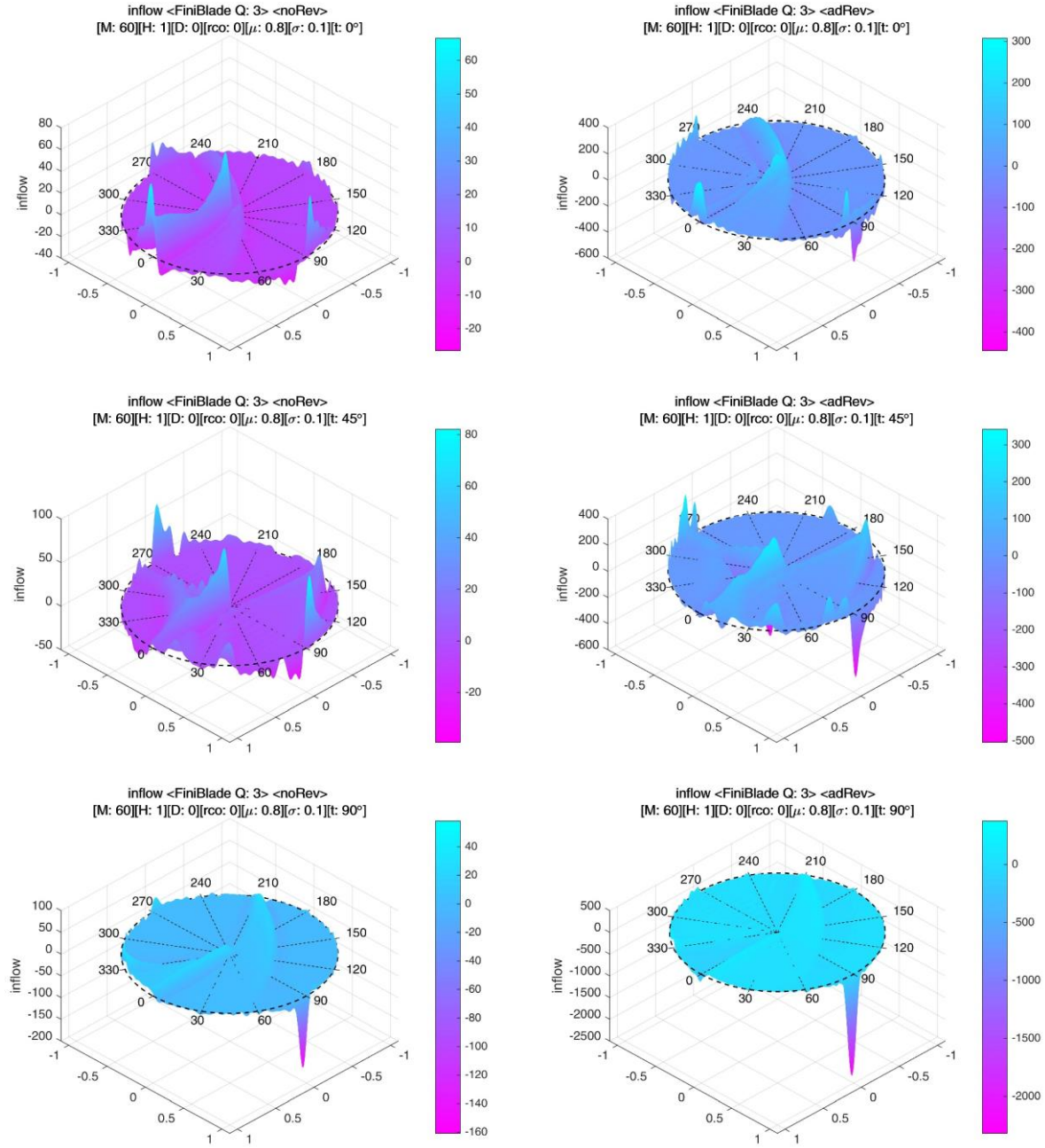


Figure 6.16. Inflow distribution both without and with reverse flow, $\mu=0.8$.

6. Summary and Conclusions

1. The Finite-state Dynamic Inflow model provides a rigorous tool for analyzing lifting rotor performance in forward flight. The model is extended to include the effects of reverse flow, inflow feedback, and number of blades.
2. For the first time, direct comparisons between the analytical finite-state approach and other numerical approaches are given, and they show similar induced power behavior.
3. The model provides optimum performance subject to specified constraints.
4. The present direct analytical method qualitatively reproduces the results found by Ormiston, Hall, and Giovanetti from numerical computation, including the singularity in normalized induced power.
5. Full solution convergence was achieved with more efficient algorithms and better conditioning enhancement than used by previous investigators.
6. With no reverse flow, moderate root cut-out reduces the induced power.
7. Reverse flow creates an infinite peak in normalized induced power due to the inability of a rotor to generate lift from collective pitch when trimmed to zero pitch and roll moments.
8. When the effect of reverse flow is added, root cut-out shifts the singularity to a higher μ .
9. The introduction of higher harmonic controls decreases induced power in all three conditions: without reverse flow, with reverse flow, and with inflow feedback and reverse flow. With a sufficient number of control degrees of freedom, the induced power approaches Glauert's minimum ideal power.
10. Higher harmonic control removes the infinite power peak caused by reverse flow.

11. Because of the way the pressure is distributed across the finite chord length, results with a finite number of blades are affected by solidity without the presence of the inflow feedback effect.
12. Higher solidity reduces the induced power for a finite-bladed rotor when there is no inflow feedback.
13. Greater inflow feedback (due to greater solidity) reduces the induced power for an infinite-bladed rotor.
14. For a rotor with a finite number of blades, the addition of inflow feedback can either increase or decrease optimum power depending on the flight conditions.

7. Possible Future Work

In this dissertation, we were interested in the maximum ideal power—not the maximum practical power. Consequently, some of the assumptions used are very idealistic. To obtain more realistic induced power, more realistic assumptions should be considered. For example, blade stall should be added to the blade element theory because realistic lift coefficients do not behave linearly with pitch angle at large angles. Similarly, blade profile drag should also be included since it is very stall dependent. The result of these two additions is that blade chord should be added as a design variable, rather than the use of a constant-chord blade. For linear lift, blade chord and blade pitch are equivalent in terms of the lift produced; but, with stall and drag, blade chord and twist will have independent effects that would need to be optimized. Next, propulsive force and external wings with wing flaps should be added to the trim controls. Future high-speed rotorcraft will no doubt unload the rotor and put some of lift, propulsion, and control on external devices. Finally, the rigid blade assumption should be relaxed so that the optimization can consider flexible blades. At the high speeds, envisioned for the future, rotorcraft will no doubt reduce blade RPM,

which will make the blades relatively softer and impose structural limits for the blade to be able to support the necessary loads.

References

- [1]. Glauert, H., "A General Theory of the Autogyro," R&M No. 1111, Aeronautical Research Council of Great Britain, March 1927.
- [2]. Harris, Franklin D., "Rotary Wing Aerodynamics Historical Perspectives and Important Issues," Proceedings of the American Helicopter Society Southwest Region National Specialists' Meeting on Aerodynamics and Aeroacoustics, Ft. Worth, Texas, February 25-27, 1987, pp 1 – 113.
- [3]. Hall, S. R., Yang, K. Y., and Hall, K. C., "Helicopter Rotor Lift Distributions for Minimum-Induced power," *Journal of Aircraft*, Vol. 1, (4), July-August 1994, pp. 837-845.
- [4]. Hall, Kenneth C. and Hall, Steven R., "A Variational Method for Computing the Optimal Aerodynamic Performance of Conventional and Compound Helicopters," *Journal of the American Helicopter Society*, Vol. 55, No. 4, October, 2010, pp. 042006-1 through 042006-16.
- [5]. Ormiston, Robert A., "Helicopter Rotor Induced Power," Proceedings of the AHS International 60th Annual Forum and Technology Display, Baltimore, MD, June 8-10, 2004.
- [6]. Ormiston, Robert A., "Further Investigations of Helicopter Rotor Induced Power," Proceedings of the AHS International 61st Annual Forum and Technology Display, Grapevine, Texas, June 1-3, 2005, SKU# : 61-2005-000267.
- [7]. Ormiston, Robert A., "A New Formulation for Lifting Rotor Performance Including Comparison with Full-Scale Data," Proceedings of the AHS International 64th Annual Forum and Technology Display, Montreal, Quebec, Canada, April 29 - May 1, 2008, SKU #: 64-2008-000184.

- [8]. Ormiston, Robert A., "An Analytical Formulation for Lifting Rotor Induced Power," Proceedings of the AHS International 65th Annual Forum and Technology Display, Grapevine, TX, May 27-29, 2009, SKU #: 65-2009-000399.
- [9]. Ormiston, Robert A., "Applications of the Induced Power Model and Performance of Conventional and Advanced Rotorcraft," Proceedings of the American Helicopter Society Aeromechanics Specialists' Conference, San Francisco, CA, January 20-22, 2010, SKU #: sm_aeromech_2010_OrmistonRa.
- [10]. Garcia-Duffy, Cristina, *Applying Dynamic Wake Models to Induced Power Calculations for an Optimum Rotor*, Doctoral Thesis 0073, Washington University in St. Louis, December 2008.
- [11]. Peters, David A. and Garcia-Duffy, Cristina, "Optimum Rotor Performance in Axial Flow by Finite-State Methods," Proceedings of the AHS International 63rd Annual Forum and Technology Display, Virginia Beach, VA, May 1-3, 2007, SKU #: 63-2007-000075.
- [12]. He, Cheng Jian, *Development and Applications of a Generalized Dynamic Wake Theory for Lifting Rotors*, Ph.D. Dissertation, Georgia Institute of Technology, August 1989.
- [13]. Makinen, S.M., *Applying Dynamic Wake Models to Large Swirl Velocities for Optimal Propellers*, Doctoral Thesis, Washington University in Saint Louis, May 2005.
- [14]. Peters, David A., File, Chad, and Ormiston, Robert A., "Rotor Performance and Optimum Power from Finite-State Inflow with Realistic Constraints," Proceedings of the 67th Annual National Forum of the American Helicopter Society, Virginia Beach, Virginia, May 3-5, 2011, SKU #: 67-2011-000261.

- [15]. File, Chad L, *Optimization of Induced-Power from Dynamic Inflow Theory*, Ph.D. Dissertation, Washington University in St. Louis, May 2013.
- [16]. Hall, Kenneth C. and Giovanetti, Eli B., “Minimum Power Requirements and Optimal Rotor Design for Conventional and Compound Helicopters Using Higher Harmonic Control,” Proceedings of the 69th Annual National Forum of the American Helicopter Society, Phoenix, Arizona, May 21–23, 2013, SKU #: 69-2013-263
- [17]. Garcia-Duffy, Cristina, Peters, David A., and Ormiston, Robert A., “Optimum Rotor Performance in Skewed Flow Based on Actuator-Disk Theory,” Proceedings of the 27th AIAA Applied Aerodynamics Conference, San Antonio, TX, June 22-25, 2009, AIAA- 2009-3517.
- [18]. Hong, JunSoo, Peters, David A., Ormiston, Robert A. “A Dynamic Inflow-Based Power Model for General and Optimal Rotor Performance,” Proceedings of the 42nd European Rotorcraft Forum, Lille, France, September 5-8, 2016, paper #45.
- [19]. Wheatley, John B. “An Aerodynamic Analysis of the Autgyro Rotor With a Comparison Between Calculated and Experimental Results,” NACA Report 487, 1934.

Appendices

Appendix A. Table Method and Rectangular Method

As the name indicates, Finite-state inflow model uses finite number of states. Solutions obtained from model become more accurate as a number of states increases. Most of Dr. Peters' previous students used table method. For the table method, users need to decide only one number which is maximum harmonic number, M. Once the M is decided, the number of polynomials, N, is automatically decided. The total number of states for the table method is $\frac{1}{2}*(M+1)*(M+2)$.

Table Method - M = 9, #states = 55							
m \ n	1	2	3	4	5	6	...
...
-10	11	13	15	17	19	21	...
-9	10	12	14	16	18	20	...
-8	9	11	13	15	17	19	...
-7	8	10	12	14	16	18	...
-6	7	9	11	13	15	17	...
-5	6	8	10	12	14	16	...
-4	5	7	9	11	13	15	...
-3	4	6	8	10	12	14	...
-2	3	5	7	9	11	13	...
-1	2	4	6	8	10	12	...
0	1	3	5	7	9	11	...
1	2	4	6	8	10	12	...
2	3	5	7	9	11	13	...
3	4	6	8	10	12	14	...
4	5	7	9	11	13	15	...
5	6	8	10	12	14	16	...
6	7	9	11	13	15	17	...
7	8	10	12	14	16	18	...
8	9	11	13	15	17	19	...

Table Method - M = 4, #states = 15							
m \ n	1	2	3	4	5	6	...
...
-10	11	13	15	17	19	21	...
-9	10	12	14	16	18	20	...
-8	9	11	13	15	17	19	...
-7	8	10	12	14	16	18	...
-6	7	9	11	13	15	17	...
-5	6	8	10	12	14	16	...
-4	5	7	9	11	13	15	...
-3	4	6	8	10	12	14	...
-2	3	5	7	9	11	13	...
-1	2	4	6	8	10	12	...
0	1	3	5	7	9	11	...
1	2	4	6	8	10	12	...
2	3	5	7	9	11	13	...
3	4	6	8	10	12	14	...
4	5	7	9	11	13	15	...
5	6	8	10	12	14	16	...
6	7	9	11	13	15	17	...
7	8	10	12	14	16	18	...
8	9	11	13	15	17	19	...

9	10	12	14	16	18	20	...
10	11	13	15	17	19	21	...
...

9	10	12	14	16	18	20	...
10	11	13	15	17	19	21	...
...

Figure A.1. How to choose states for table method

For example, if M=4 then the total number of states is 15.

$$\{\tau\}_{\text{w table method}} = \left[\tau_5^{-4} \quad \tau_4^{-3} \quad \tau_3^{-2} \quad \tau_5^{-2} \quad \tau_2^{-1} \quad \tau_4^{-1} \quad \tau_1^{-0} \quad \tau_3^0 \quad \tau_5^0 \quad \tau_2^1 \quad \tau_4^1 \quad \tau_3^2 \quad \tau_5^2 \quad \tau_4^3 \quad \tau_5^4 \right]^T$$

Rectangular method requires users to pick two numbers: maximum harmonics, and number of polynomial. The total number of states for the rectangular method is $[(M*2)+1]*N$.

Rectangular Method - M = 9, N = 5, #states = 95								
n \ m	1	2	3	4	5	6	7	...
...
-10	11	13	15	17	19	21	23	...
-9	10	12	14	16	18	20	22	...
-8	9	11	13	15	17	19	21	...
-7	8	10	12	14	16	18	20	...
-6	7	9	11	13	15	17	19	...
-5	6	8	10	12	14	16	18	...
-4	5	7	9	11	13	15	17	...
-3	4	6	8	10	12	14	16	...
-2	3	5	7	9	11	13	15	...
-1	2	4	6	8	10	12	14	...
0	1	3	5	7	9	11	13	...
1	2	4	6	8	10	12	14	...
2	3	5	7	9	11	13	15	...
3	4	6	8	10	12	14	16	...
4	5	7	9	11	13	15	17	...
5	6	8	10	12	14	16	18	...
6	7	9	11	13	15	17	19	...
7	8	10	12	14	16	18	20	...
8	9	11	13	15	17	19	21	...
9	10	12	14	16	18	20	22	...
10	11	13	15	17	19	21	23	...
...

Rectangular Method - M = 3, N = 2, #states = 14								
n \ m	1	2	3	4	5	6	7	...
...
-10	11	13	15	17	19	21	23	...
-9	10	12	14	16	18	20	22	...
-8	9	11	13	15	17	19	21	...
-7	8	10	12	14	16	18	20	...
-6	7	9	11	13	15	17	19	...
-5	6	8	10	12	14	16	18	...
-4	5	7	9	11	13	15	17	...
-3	4	6	8	10	12	14	16	...
-2	3	5	7	9	11	13	15	...
-1	2	4	6	8	10	12	14	...
0	1	3	5	7	9	11	13	...
1	2	4	6	8	10	12	14	...
2	3	5	7	9	11	13	15	...
3	4	6	8	10	12	14	16	...
4	5	7	9	11	13	15	17	...
5	6	8	10	12	14	16	18	...
6	7	9	11	13	15	17	19	...
7	8	10	12	14	16	18	20	...
8	9	11	13	15	17	19	21	...
9	10	12	14	16	18	20	22	...
10	11	13	15	17	19	21	23	...
...

Figure A.2. How to choose states for rectangular method

For example, if $M=3$ and $N=2$, then the total number of states is 14.

$$\{\tau\}_{\text{w rectangular method}} = \left[\tau_4^{-3} \quad \tau_6^{-3} \quad \tau_3^{-2} \quad \tau_5^{-2} \quad \tau_2^{-1} \quad \tau_4^{-1} \quad \tau_1^0 \quad \tau_3^0 \quad \tau_2^1 \quad \tau_4^1 \quad \tau_3^2 \quad \tau_5^2 \quad \tau_4^3 \quad \tau_6^3 \right]^T$$

Conversion Comparison for Infinite Number of Blades without reverse flow is shown in figures below.

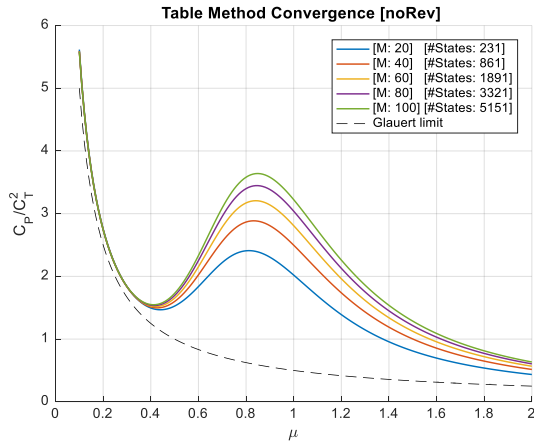


Figure A.3. Table method convergence without reverse flow for an infinite number of blades

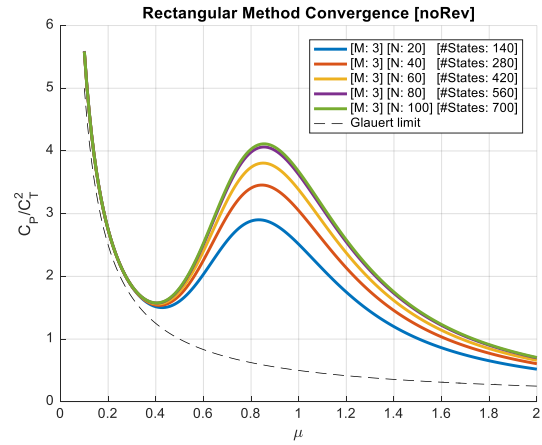


Figure A.4. Rectangular method convergence without reverse flow for an infinite number of blades

Figures A.3 and A.4 shows that the induced power conversion trend for table and rectangular method for an infinite number of blades. While Fig. A.3 uses 5151 states, Fig. A.4 uses 700 states as its maximum total number of states. Comparisons of Figs. A.3 and A.4 show that the rectangular method converges faster than the table method does for an infinite number of blades. For a finite number of blade, the rectangular method converges faster than the table method does.

Appendix B. Real Notation to Complex Notation

$$\begin{bmatrix} \ddots & & \\ & G_n^m & \\ & & \ddots \end{bmatrix} \{\dot{\gamma}_j^r\} + 2V \begin{bmatrix} L_j^r & m \\ & n \end{bmatrix} \{\gamma_j^r\} = \{\tau_n^m\}$$

$$\cos(x) = \text{Re}(e^{ix}) = \frac{e^{ix} + e^{-ix}}{2} \quad \sin(x) = \text{Im}(e^{ix}) = \frac{e^{ix} - e^{-ix}}{2i}$$

Inflow Distributions

$$\omega(\bar{r}, \psi, t) = \alpha_n^{mc}(t) \cos(r\psi) \frac{\bar{P}_j^r}{\nu}(\nu) + \beta_n^{ms}(t) \sin(r\psi) \frac{\bar{P}_j^r}{\nu}(\nu) \text{ (Real Notation)}$$

$$\begin{aligned} &= \phi_j^r(\bar{r}) \left[\alpha_j^r(t) \left(\frac{e^{ir\psi} + e^{-ir\psi}}{2} \right) + \beta_j^r(t) \left(\frac{e^{ir\psi} - e^{-ir\psi}}{2i} \right) \right] \\ &= \phi_j^r(\bar{r}) \left[\alpha_j^r(t) \left(\frac{e^{ir\psi} + e^{-ir\psi}}{2} \right) + i\beta_j^r(t) \left(\frac{-e^{ir\psi} + e^{-ir\psi}}{2} \right) \right] \\ &= \frac{1}{2} \phi_j^r(\bar{r}) \left[e^{ir\psi} (\alpha_j^r(t) - i\beta_j^r(t)) + e^{-ir\psi} (\alpha_j^r(t) + i\beta_j^r(t)) \right] \\ &= \phi_j^r(\bar{r}) \left[e^{ir\psi} \frac{1}{2} (\alpha_j^r(t) - i\beta_j^r(t)) + e^{-ir\psi} \frac{1}{2} (\alpha_j^r(t) + i\beta_j^r(t)) \right] \end{aligned}$$

$$\text{(Change of Variables)} \quad \therefore \gamma_j^r \cdot e^{i\ell t} = \frac{1}{2} [(\alpha_j^r(t) - i\beta_j^r(t))] \quad \therefore \gamma_j^{-r} \cdot e^{i\ell t} = \frac{1}{2} [(\alpha_j^r(t) + i\beta_j^r(t))]$$

$$\begin{aligned} &= \phi_j^r(\bar{r}) [e^{ir\psi} \cdot \gamma_j^r + e^{-ir\psi} \cdot \gamma_j^{-r}] \cdot e^{i\ell t} \\ &= \sum_{r=-\infty}^{+\infty} \phi_j^r(\bar{r}) \gamma_j^r \cdot e^{ir\psi} \cdot e^{i\ell t} \end{aligned}$$

$$\omega(\bar{r}, \psi, \bar{t}) = \sum_{\ell=-\infty}^{+\infty} \sum_{r=-\infty}^{+\infty} \sum_{j=|r|+1, |r|+3, \dots}^{rMax+1} \phi_j^r(\bar{r}) \{\gamma_j^r\}_{\ell} \cdot e^{ir\psi} \cdot e^{i\ell t} \quad (\text{Complex Notation})$$

Pressure Distributions

$$\Delta P(\bar{r}, \psi, t) = \bar{P}_n^m(\nu) \left(\tau_n^{mc}(t) \cos(m\psi) + \tau_n^{ms}(t) \sin(m\psi) \right) \quad (\text{Real Notation})$$

$$(\text{Change of Variables}) \quad \therefore \tau_n^m \cdot e^{ikt} = \frac{1}{2} \left[\left(\tau_n^{mc}(t) - i\tau_n^{ms}(t) \right) \right] \quad \therefore \tau_n^{-m} \cdot e^{ikt} = \frac{1}{2} \left[\left(\tau_n^{mc}(t) + i\tau_n^{ms}(t) \right) \right]$$

$$\Delta P(\bar{r}, \psi, \bar{t}) = \sum_{k=-\infty}^{+\infty} \sum_{m=-\infty}^{+\infty} \sum_{n=|m|+1, |m|+3, \dots}^{mMax+1} \bar{P}_n^m(\nu) \{\bar{\tau}_n^m\}_k \cdot e^{im\psi} \cdot e^{ik\bar{t}} \quad (\text{Complex Notation})$$

Rotor Controls

$$\theta(\bar{r}, \psi_q) = \sum_{k=0}^K \sum_{m=0}^M \left[\bar{r}^p \left[\theta_m^k \cdot \cos(k\psi_q) + \theta_m^k \cdot \sin(k\psi_q) \right] \right] \quad (\text{Real Notation})$$

$$(\text{Change of Variables}) \quad \therefore \theta_d^h = \frac{1}{2} \left[\left(\theta_m^k - i\theta_m^k \right) \right] \quad \therefore \theta_d^{-h} = \frac{1}{2} \left[\left(\theta_m^k + i\theta_m^k \right) \right]$$

$$\theta(\bar{r}, \psi_q) = \sum_{h=-H}^{+H} \sum_{d=0}^D \bar{r}^d \bar{\theta}_d^h e^{ih\psi_q} \quad (\text{Complex Notation})$$

D Matrix

$$\begin{Bmatrix} C_T \\ C_L \\ C_M \end{Bmatrix} = \begin{bmatrix} 2/\sqrt{3} & 0 & 0 \\ 0 & 0 & -\sqrt{2/15} \\ 0 & -\sqrt{2/15} & 0 \end{bmatrix} \begin{Bmatrix} \tau_1^{0c} \\ \tau_2^{1c} \\ \tau_2^{1s} \end{Bmatrix} \quad (\text{Real Notation})$$

$$(\text{Change of Variables}) \quad \therefore \begin{Bmatrix} \tau_1^{0c} \\ \tau_2^{1c} \\ \tau_2^{1s} \end{Bmatrix} = \begin{bmatrix} 0 & 1 & 0 \\ 1 & 0 & 1 \\ -i & 0 & i \end{bmatrix} \begin{Bmatrix} \tau_2^{-1} \\ \tau_1^0 \\ \tau_2^1 \end{Bmatrix}$$

$$\begin{Bmatrix} C_T \\ C_L \\ C_M \end{Bmatrix} = \begin{bmatrix} 2/\sqrt{3} & 0 & 0 \\ 0 & 0 & -\sqrt{2/15} \\ 0 & -\sqrt{2/15} & 0 \end{bmatrix} \begin{bmatrix} 0 & 1 & 0 \\ 1 & 0 & 1 \\ -i & 0 & i \end{bmatrix} \begin{Bmatrix} \tau_2^1 \\ \tau_1^0 \\ \tau_2^1 \end{Bmatrix}$$

$$\begin{Bmatrix} C_T \\ C_L \\ C_M \end{Bmatrix} = \begin{bmatrix} 0 & 2/\sqrt{3} & 0 \\ i\sqrt{2/15} & 0 & -i\sqrt{2/15} \\ -\sqrt{2/15} & 0 & -\sqrt{2/15} \end{bmatrix} \begin{Bmatrix} \tau_2^{-1} \\ \tau_1^0 \\ \tau_2^1 \end{Bmatrix} \quad (\text{Complex Notation})$$

Appendix C. Simplification of Eq. (2.6.5) to Eq. (2.6.7)

$$\{\tau\} = \frac{\sigma a}{4} \cdot [[A]\{\theta\} - [B]\{\gamma\}] \quad \rightarrow \quad \{\tau\} = \frac{\sigma a}{4} \cdot \left[[I] + \frac{\sigma a}{8V} [B][L] \right]^{-1} [A]\{\theta\}$$

Substitution of Eq. (2.6.5), $\{\gamma_n^m\} = \left(\frac{1}{2V}\right) \cdot [L]\{\tau_n^m\}$, into Eq. (2.6.5)

$$(C.1) \quad \{\tau\} = \frac{\sigma a}{4} \cdot \left[[A]\{\theta\} - [B]\{\gamma\} \right] \quad (2.6.5)$$

$$(C.2) \quad \{\tau\} = \frac{\sigma a}{4} \cdot \left[[A]\{\theta\} - [B]\left(\frac{1}{2V}\right) \cdot [L]\{\tau\} \right]$$

$$(C.3) \quad \{\tau\} = \frac{\sigma a}{4} [A]\{\theta\} - \frac{\sigma a}{8V} [B][L]\{\tau\}$$

$$(C.4) \quad \{\tau\} + \frac{\sigma a}{8V} [B][L]\{\tau\} = \frac{\sigma a}{4} [A]\{\theta\}$$

$$(C.5) \quad \{\tau\} \left[[I] + \frac{\sigma a}{8V} [B][L] \right] = \frac{\sigma a}{4} [A]\{\theta\}$$

$$(C.6) \quad \{\tau\} = \frac{\sigma a}{4} \left[[I] + \frac{\sigma a}{8V} [B][L] \right]^{-1} [A]\{\theta\} \quad (2.6.7)$$

Appendix D. Determinant of Wheatley Terms

The terms found by Wheatley¹⁹ for thrust and roll moment (for the condition $\mu \leq 1$) are given below, in which the second bracketed term in each line is the effect of reverse flow. These terms can also be found in Ref. 19, page 42.

$$\begin{aligned}
 \frac{C_T}{\sigma a} &= \frac{1}{2\pi} \int_0^{2\pi} \int_0^1 \frac{1}{2} (r + \mu \sin \psi)^2 (\theta_0 + \theta_s \sin \psi) \cdot dr \cdot d\psi \\
 &\quad - \frac{1}{2\pi} \int_\pi^{2\pi} \int_0^{-\mu \sin \psi} (r + \mu \sin \psi)^2 (\theta_0 + \theta_s \sin \psi) \cdot dr \cdot d\psi \\
 -\frac{C_L}{\sigma a} &= \frac{1}{2\pi} \int_0^{2\pi} \int_0^1 \frac{1}{2} (r + \mu \sin \psi)^2 (\theta_0 + \theta_s \sin \psi) (r \sin \psi) \cdot dr \cdot d\psi \\
 &\quad - \frac{1}{2\pi} \int_\pi^{2\pi} \int_0^{-\mu \sin \psi} (r + \mu \sin \psi)^2 (\theta_0 + \theta_s \sin \psi) (r \sin \psi) \cdot dr \cdot d\psi
 \end{aligned} \tag{D.1}$$

$$\begin{aligned}
 \frac{C_T}{\sigma a} &= \frac{1}{12} \left[(3\mu^2 + 2)\theta_0 + 3\mu\theta_s \right] - \left[\frac{\mu^3 (32\theta_0 - 9\pi\theta_s)}{144\pi} \right] \\
 -\frac{C_L}{\sigma a} &= \frac{[16\mu\theta_0 + (9\mu^2 + 6)\theta_s]}{96} - \left[-\frac{2\mu^4\theta_0}{45\pi} + \frac{5\mu^4\theta_s}{384} \right]
 \end{aligned} \tag{D.2}$$

[Wheatley acknowledges that he neglected some of the reverse flow terms in the roll moment. As a consequence, in the terms reported in Ref. 19, the last term in the second line above is incorrectly given as $(3\mu^4/32)\theta_s$.] Equation (D.2) can be rearranged to give:

$$\begin{aligned}\frac{C_T}{\sigma a} &= \left(-\frac{2}{9\pi}\mu^3 + \frac{1}{4}\mu^2 + \frac{1}{6}\right)\theta_0 + \left(\frac{1}{16}\mu^3 + \frac{1}{4}\mu\right)\theta_s \\ -\frac{C_L}{\sigma a} &= \left(\frac{2}{45\pi}\mu^4 + \frac{1}{6}\mu\right)\theta_0 + \left(-\frac{5}{384}\mu^4 + \frac{3}{32}\mu^2 + \frac{1}{16}\right)\theta_s\end{aligned}\tag{D.3}$$

$$\begin{aligned}\frac{6 \cdot C_T}{\sigma a} &= \left(-\frac{4}{3\pi}\mu^3 + \frac{3}{2}\mu^2 + 1\right)\theta_0 + \left(\frac{3}{8}\mu^3 + \frac{3}{2}\mu\right)\theta_s \\ -\frac{16 \cdot C_L}{\sigma a} &= \left(\frac{32}{45\pi}\mu^4 + \frac{8}{3}\mu\right)\theta_0 + \left(-\frac{5}{24}\mu^4 + \frac{3}{2}\mu^2 + 1\right)\theta_s\end{aligned}\tag{D.4}$$

Equation (D.4) represents the trim equations, which can be expressed in matrix form as:

$$\begin{Bmatrix} \frac{6 \cdot C_T}{\sigma a} \\ -\frac{16 \cdot C_L}{\sigma a} \end{Bmatrix} = \begin{bmatrix} 1 + \frac{3}{2}\mu^2 - \frac{4}{3\pi}\mu^3 & \frac{3}{2}\mu + \frac{3}{8}\mu^3 \\ \frac{8}{3}\mu + \frac{32}{45\pi}\mu^4 & 1 + \frac{3}{2}\mu^2 - \frac{5}{24}\mu^4 \end{bmatrix} \begin{Bmatrix} \theta_0 \\ \theta_s \end{Bmatrix}\tag{D.5}$$

The determinant of the right-hand side of Eq. (D.5) gives the advance ratio at which Wheatley predicts the system is no longer trimmable and where power goes to infinity.

$$Det = 1 - \mu^2 - \frac{4}{3\pi}\mu^3 + \frac{25}{24}\mu^4 - \frac{46}{15\pi}\mu^5 - \frac{5}{16}\mu^6 - \frac{1}{90\pi}\mu^7\tag{D.6}$$

$$\mu \approx 0.853120\tag{D.7}$$

The first root of this equation is $\mu = 0.853120$, which is the theoretical, critical advance ratio where trim is not possible using only collective and cyclic pitch.

Appendix E. Complex Version of [L] Matrix

Peters and He developed complex version of [L] matrix but never published their result through journals. Complex version of [L] matrix was crucial tool for obtaining induced power for a finite number of blades because algebra became much simpler by using it. Below equations are definitions of complex [L] matrix and components inside of [L] matrix.

$$\left[L_{jn}^{rm} \right] = (-1)^{\frac{|m|+|r|-|m+r|}{2}} X^{|m-r|} \left[\Gamma_{jn}^{rm} \right]$$

$$X = \tan\left(\chi/2\right)$$

χ = wake skew angle ($\chi = 87.5^\circ$ for this thesis)

$$\begin{aligned} \Gamma_{jn}^{rm} &= \frac{(-1)^{\frac{n+j-2r}{2}}}{\sqrt{H_n^m H_j^r}} \frac{2\sqrt{(2n+1)(2j+1)}}{(j+n)(j+n+2)[(j-n)^2-1]} & \text{for } r+m \text{ even} \\ \Gamma_{jn}^{rm} &= \frac{\pi}{2\sqrt{H_n^m H_j^r}} \frac{\text{sgn}(r-m)}{\sqrt{(2n+1)(2j+1)}} & \text{for } r+m \text{ even} \\ \Gamma_{jn}^{rm} &= 0 & \text{for } r+m \text{ even} \end{aligned}$$

$$H_n^m = \frac{(n+m-1)!!(n-m-1)!!}{(n+m)!!(n-m)!!}$$

Vita

Date of Birth	Sep 23, 1989
Place of Birth	Seoul, Korea
Degrees	Ph.D. Mechanical Engineering, August 2017 M.S. Aerospace Engineering, May 2017 M.S. Mechanical Engineering, May 2015 B.S. Mechanical Engineering, May 2013 All obtained from Washington University in St. Louis
Professional Societies	American Helicopter Society (AHS) American Institute of Aeronautics and Astronautics (AIAA)
Honors	Runner-up for Robert L. Lichten award
Publications	Hong, JunSoo; Peters, David A; “Minimum Induced Power for a Rotor with a Finite Number of Blades”, <i>Journal of Aircraft</i> , In press. Hong, JunSoo; Peters, David A; Ormiston, Robert A., “A Dynamic-Inflow Based Induced Power Model for General and Optimal Rotor Performance”, <i>Journal of American Helicopter Society</i> , In press. Hong, JunSoo; Peters, David A; Ormiston, Robert A., “A Dynamic Inflow-Based Induced Power Model for General and Optimal Rotor Performance” Proceedings of the 42nd European Rotorcraft Forum, Lille, France, September 5-8, 2016 Hong, JunSoo “A Fully Nonlinear Version of the Pitt-Peter Dynamic Inflow Model in Axial Flow” Proceedings of the AHS International 69th Annual Forum and Technology Display, Phoenix, Arizona, May 21-23, 2013